

1 **Aberrant hippocampal transmission and behavior in mice with a** 2 **stargazin mutation linked to intellectual disability**

3 Caldeira GL^{*,1,2,3}, Inácio AS^{*,1,2}, Beltrão N^{1,2,3}, Barreto CAV^{1,2,3}, Rodrigues MV^{1,2,3},
4 Rondão T¹, Macedo R^{1,4}, Gouveia RP^{1,4}, Edfawy M^{1,2,3,&}, Guedes J^{1,2}, Cruz B^{1,4,#}, Louros
5 SR^{1,2,§}, Moreira IS^{1,4}, Peça J^{1,4}, Carvalho AL^{1,4,||}

6 ¹CNC-Center for Neuroscience and Cell Biology, University of Coimbra, 3004-504
7 Coimbra, Portugal.

8 ²IIIUC-Institute for Interdisciplinary Research, University of Coimbra, 3030-789 Coimbra,
9 Portugal.

10 ³PhD Program in Experimental Biology and Biomedicine (PDBEB), University of
11 Coimbra, Portugal

12 ⁴Department of Life Sciences, University of Coimbra, 3000-456 Coimbra, Portugal.

13 *These authors contributed equally to this work.

14 #Current address: Champalimaud Research, Champalimaud Centre for the Unknown,
15 Lisbon, Portugal

16 §Current address: Centre for Discovery Brain Sciences, University of Edinburgh, UK

17 &Current address: HEMEX AG, Liestal, Switzerland

18 ||Corresponding author: alc@cnc.uc.pt (Ana Luisa Carvalho)

19

20 **Running title:** ID-associated stargazin mutation impairs hippocampal synaptic
21 transmission

22 **Keywords:** Transmembrane AMPAR regulatory proteins; stargazin; intellectual
23 disability; dendritic spines; hippocampal synaptic transmission

24 **ABSTRACT**

25 Mutations linked to neurodevelopmental disorders, such as intellectual disability (ID), are
 26 frequently found in genes that encode for proteins of the excitatory synapse.
 27 Transmembrane AMPA receptor regulatory proteins (TARPs) are AMPA receptor
 28 auxiliary proteins that regulate crucial aspects of receptor function. Here, we investigate
 29 an ID-associated mutant form of the TARP family member stargazin. Molecular
 30 dynamics analyses showed that the stargazin V143L variant weakens the overall
 31 interface of the AMPAR:stargazin complex and hinders the stability of the complex.
 32 Knock-in mice for the V143L stargazin mutation manifest cognitive and social deficits
 33 and hippocampal synaptic transmission defects. In the hippocampus of stargazin V143L
 34 mice, CA1 neurons show impaired spine maturation in basal dendrites, and synaptic
 35 ultrastructural alterations. These data demonstrate a causal role for mutated stargazin
 36 in the pathogenesis of ID and highlight its role in the development and function of
 37 hippocampal synapses.

38

39 INTRODUCTION

40 Most of the fast component of excitatory neurotransmission in the central nervous
41 system is mediated by glutamate receptors of the α -amino-3-hydroxyl-5-methyl-4-
42 isoxazole-propionate type (AMPA). This family of receptors is associated with receptor
43 auxiliary proteins that regulate their traffic, gating and pharmacology, thus increasing
44 receptor functional diversity in the brain ¹⁻³. Members of the transmembrane AMPAR
45 regulatory protein (TARP) family are widely expressed AMPAR auxiliary subunits ⁴, and
46 key modulators of AMPAR-mediated transmission. The prototypical TARP stargazin
47 (also known as TARP γ 2) was discovered in the ataxic stargazer mouse ⁵, which lacks
48 synaptic AMPARs on cerebellar granule cells ⁶. Stargazin interacts with both AMPA
49 receptor subunits and synaptic PDZ-containing proteins such as postsynaptic density
50 protein 95 [PSD95; ⁷], and this is required for targeting AMPAR to synapses ^{7,8}. The
51 stargazin/PSD95 complex has recently been found to form a condensed assembly via
52 liquid-liquid phase separation, a process that is critical for AMPAR-mediated
53 transmission ⁹.

54 TARPs, including stargazin, couple with the majority of AMPAR complexes in the brain,
55 promote receptor trafficking to the cell surface and their synaptic targeting, and augment
56 their functional properties ^{1,2}. Stargazin slows the rates of AMPAR desensitization and
57 deactivation thus increasing the size of the postsynaptic current. Not surprisingly,
58 stargazin regulates baseline synaptic transmission and is also involved in Hebbian and
59 homeostatic forms of synaptic plasticity that are dependent on tightly regulated AMPAR
60 traffic ¹⁰⁻¹².

61 Impaired glutamatergic synaptic transmission and plasticity have been implicated in
62 neurodevelopmental disorders ¹³. Evidence from human genetic studies suggests that
63 copy number variation or the presence of rare point mutations in genes encoding proteins
64 of the ionotropic glutamate receptor complex may play a role in the aetiology of these

disorders¹⁴⁻¹⁸. Single nucleotide polymorphisms in the *CACNG2* gene encoding stargazin were associated with a subgroup of schizophrenia patients¹⁹, and alterations in the DNA copy number and in the levels of stargazin mRNA were detected in the post-mortem brain of schizophrenia patients^{20,21}. Dysregulated stargazin expression was also found in the dorsolateral prefrontal cortex of patients with bipolar disorder²¹, and stargazin polymorphisms were associated with the response to lithium, a frequent treatment for bipolar disorder^{21,22}. A *de novo* missense mutation in *CACNG2* has been identified in a non-syndromic intellectual disability (ID) patient with moderate severity¹⁶. Taken together, these data point to a possible link between stargazin and the pathogenesis of neurodevelopmental disorders, which has not yet been investigated. Evaluating how human mutations in the stargazin-encoding gene disrupt synaptic function and impact behavior may also provide insight into the physiological role of stargazin.

Here, we investigated the impact of the ID-associated missense V143L mutation in stargazin¹⁶ in the molecular dynamics (MD) of the AMPAR:stargazin complex, in the cell surface diffusion of stargazin and in its ability to traffic AMPAR to the neuronal surface and to the synapse. To evaluate behavioral, neuronal morphology and functional alterations triggered by the stargazin V143L variant, we generated a knock-in (KI) mouse model to express the mutant protein. We found that stargazin V143L KI mice display alterations in cognitive and social behavior, along with altered hippocampal spine morphology, associated with synaptic ultrastructural defects. We also found disrupted synaptic transmission and aberrant stargazin phosphorylation in stargazin V143L mutant mice.

88

89 RESULTS

90 Intellectual disability-associated stargazin V143L mutation affects the 91 AMPAR:stargazin complex structure

92 A *de novo* missense mutation in the *CACNG2* gene encoding stargazin was described
93 in a heterozygous 8 year-old male patient with moderate, non-syndromic, intellectual
94 disability ¹⁶. This mutation leads to substitution of valine143 by leucine (p.V143L), a
95 residue in the third transmembrane domain of stargazin that is highly conserved among
96 species (Figs. 1a,c), suggesting a critical role for the function of stargazin. Accordingly,
97 the V143L substitution was predicted to be damaging using PolyPhen-2 ²³, SIFT ²⁴ and
98 PROVEAN ²⁵. Importantly, the stargazin V143L variant has not been described in
99 databases collecting sequencing variants for the general population (Genome
100 Aggregation Database or Exome Variant Server).

101 In order to characterize the effect of the V143L stargazin mutation in the structure and
102 dynamics of the AMPAR:stargazin complex, we used molecular dynamics (MD)
103 simulations. MD simulations are key to attain an atomistic understanding of biomolecular
104 processes from ligand-binding to protein-coupling induced conformational changes, and
105 are widely used to interpret experimental data or/and to guide experimental work ^{26,27}.
106 Nevertheless, to the best of our knowledge, possibly due to the high number of residues
107 involved, there are no MD studies available regarding AMPAR:TARP complexes. To
108 perform the first MD study on this complex, we took advantage of increasing availability
109 of structural data, along with more readily accessible computational resources, to apply
110 MD algorithms and predict *in silico* how the AMPAR:stargazin system responds to a
111 particular perturbation. To this purpose we used homology modeling (Fig. 1b) to
112 construct both the WT and V143L models of the AMPAR:stargazin complex, based on
113 one of the described cryo-EM structures for the complex ²⁸.

114 AMPARs are composed of variable multidomain subunits (GluA1-GluA4, Fig. 1d)
 115 arranged in a “Y” shape, divided into three layers: the amino-terminal domains (ATDs),
 116 the ligand-binding domains (LBDs), and the transmembrane domain (TMD). TMDs, with
 117 four helices (M1-M4), show a pseudo-fourfold symmetric structure, a two-fold rotational
 118 symmetry formed by two dimers composed of A/D and B/C subunits, providing high
 119 conformational flexibility^{29,30}. As such, AMPAR:TARPs shows variable stoichiometry
 120 with an apparent maximum of four TARPs that can be broken down into two groups:
 121 TARPs binding X sites (common interfaces with AMPAR subunits A/B or C/D) and Y
 122 sites (involving subunits A/D or B/C)^[30], Fig. 1b]. We will herein refer to the GluA structure
 123 exhibiting the highest contact surface with the coupled TARP as *Main GluA* and *Auxiliary*
 124 *GluA* to the other one. We analyzed the effect of the stargazin V143L mutation at both
 125 sites taking into account different metrics on macromolecular rearrangements such as
 126 cross-correlation analysis (CCA) and root mean square deviations (RMSD), and also at
 127 the interfacial level (solvent accessible surface area - SASA).

128 Figure 1e reveals the network of correlated/anticorrelated (same/opposite direction)
 129 motions between different regions of the the AMPAR:stargazin complex structure, which
 130 informs on the impact of the stargazin V143L mutation in the overall structural
 131 conformation of the macromolecular complex. The dynamics between X and Y sites are
 132 distinct. The loops between TMD1-TMD2 and TMD3-TMD4 in stargazin are highly
 133 anticorrelated with the rest of the structure, whereas in the X site the movements are
 134 widely positively correlated. In the *Main GluA*, LBD-D1 and LBD-D2 are anticorrelated
 135 for the Y site and positively correlated for the X site. In the stargazin V143L system these
 136 differences are attenuated. In the complex containing stargazin V143L, both sites are
 137 much closer to the Y site’s motions of the complex containing the WT protein. Correlation
 138 analysis for the complete system shows a positive correlation between M1-M2-M3 of
 139 *Main GluA* and M4 of the *Auxiliary GluA* with the transmembrane regions of stargazin in
 140 both X and Y sites. This correlation weakens and, in some regions, shifts to an

141 anticorrelation with the introduction of the V143L stargazin mutation, especially in the
142 M2-M3 of *Main GluA* and M4 of *Auxiliary GluA* (observed in both sites). In the Y site, the
143 β 1- β 4 region in stargazin displays a stronger positive correlation with the D2 of the *Main*
144 *GluA* when compared to the X site, which is also weakened in the mutated system.
145 Finally, in the Y site, stargazin has a slight positive correlation with the *Auxiliary GluA*
146 transmembrane domain that is lost in the mutated systems. In the X site this correlation
147 is never present. Overall CCA results indicate that the X site is more prone to
148 conformational rearrangements introduced by the V143L mutation in stargazin than the
149 Y site.

150 RMSD was used to assess protein conformational changes between different time points
151 in the trajectory, and their distribution is shown in Figures S1 and S2 for all monomers
152 at both sites, in the WT and mutated complexes. Comparing WT- and V143L stargazin-
153 containing mutated complexes, the maximum RMSD values do not change significantly,
154 but their density is lower for lower values in the complex containing stargazin V143L,
155 demonstrating a higher flexibility. RMSD values for stargazin main substructures, α -
156 helices and β -strands, are illustrated in Figures S2a and S2b, respectively. TMD3 and
157 TMD4 show higher density for lower RMSD values, and therefore lower conformational
158 flexibility in the mutated system. In the case of the β -strands, their RMSD values were
159 higher for the mutated system at both sites, which shows a higher conformational
160 flexibility of this system, especially for β 4 and β 5. For GluA, at both X and Y sites, the
161 M1 and M2 show higher deviation and conformational flexibility in the mutated systems,
162 while M3 and M4 show lower deviation and flexibility, particularly for the mutated X site.

163 The effect of the V143L stargazin mutation on the size of the coupling interface between
164 stargazin and AMPAR was further assessed by measuring the sum of all residues SASA
165 (Figs. S3 and S4). For both sites and systems, M1 in the *Main GluA* and M4 in the
166 *Auxiliary GluA* display the lowest Δ SASA values (highest contribution) in the TM region,
167 with M1 presenting a different behavior between the two sites (data not shown). In

168 stargazin, the substructures with the highest contribution for the interface were TMD3
169 and TMD4 in the TM region (data not shown). When comparing average values per
170 substructure in the WT and V143L mutant forms of stargazin, the LBD_D2 of *Auxiliary*
171 *GluA*, $\beta 4$ of *stargazin* and the loops regions show significant differences (Fig. S3).
172 Analysis of Δ SASA per component of the interface (*Main GluA*, *Auxiliary GluA* and
173 stargazin) shows significant dissimilarities for stargazin in the X site, and for *Main GluA*
174 in the Y site (Fig. S4).

175 Taken together, the MD analysis indicates that the V143L mutation in stargazin weakens
176 the interaction of stargazin with the AMPAR complex, particularly in the X interaction site.

177

178 **The V143L mutation affects the trafficking properties of stargazin**

179 Stargazin plays a role in AMPAR trafficking through the early compartments of the
180 biosynthetic pathway ³¹, and mediates complexed AMPAR trafficking to the cell
181 membrane, their synaptic stabilization ^{7,32} and surface diffusion trapping ^{8,33} through
182 binding to PSD95. Given the described roles, we explored the potential effect of the
183 V143L mutation on stargazin's cell surface diffusion properties. Low-density cortical
184 neurons were co-transfected with plasmids encoding Homer-GFP, for synapse
185 identification, and HA-tagged WT stargazin (StgWT), or the V143L stargazin variant
186 (StgV143L). We monitored stargazin diffusion by single nanoparticle imaging of HA-
187 stargazin using quantum dots (QDs) (Figs. 2a,b). Stargazin V143L particles displayed
188 increased mean square displacement (MSD) (Fig. 2c), decreased synapse residence
189 time (Fig. 2d) and higher global and synaptic diffusion coefficients than StgWT (Figs.
190 2e,f), suggesting that the V143L mutation renders stargazin more mobile in the plasma
191 membrane.

192 The ID-associated mutation is located in the third transmembrane domain of stargazin
193 (Fig. 1c), which was shown to be involved in the interaction with AMPAR subunits ^{34,35}.

Our molecular dynamics analyses indicate that this mutation weakens the interaction of stargazin with the AMPAR complex, in particular in the X site (Fig. 1e). We thus hypothesized that stargazin V143L may be defective in trafficking AMPAR to the cell surface and to the synapse. To test this possibility, we used a molecular replacement strategy in which we silenced endogenous stargazin expression in cultured cortical neurons and re-introduced either WT stargazin or the V143L variant. We assessed the effect of stargazin depletion and of the expression of the stargazin V143L variant in AMPAR trafficking and synaptic stabilization in young (Figs. 2g-i) and mature neurons (Figs. 2j-l). Low density rat cortical neurons were transfected with a control shRNA (CTR) or with a specific shRNA that depletes the levels of endogenous stargazin [KD; ¹¹]. Cell surface and synaptic expression levels of AMPAR were evaluated by immunolabeling GluA AMPAR subunits using an antibody specific for their extracellular N-terminal region (Figs. 2g-l). As previously described ¹¹, stargazin silencing led to a decrease on the cell surface (Figs. 2h,k) and synaptic levels of AMPAR (Figs. 2i,l). AMPAR clusters were considered synaptic when colocalizing with PSD95, whose expression was not affected by stargazin silencing (data not shown). In cells co-transfected with stargazin shRNA and WT shRNA-refractory stargazin (KD + StgWT), total and synaptic surface levels of GluA were rescued to basal levels. Critically, neuronal transfection of shRNA-refractory stargazin V143L mutant (KD + Stg^{V143L}) led to a failure in mediating normal AMPAR traffic to the cell surface (Figs. 2h,k) and to the synapse (Figs. 2i,l), showing that the ID-associated mutation impairs stargazin's role in AMPAR trafficking in both young and mature neurons.

216

217 **Genetically engineered mice with the stargazin V143L mutation show altered** 218 **cognitive and social behavior**

In order to study the effects of the ID-associated stargazin mutation *in vivo*, we generated a knock-in (KI) mouse line in which the human mutation was introduced in the mouse

221 *Cacng2* gene. Using the gene targeting strategy we targeted the *Cacng2* gene to modify
 222 the nucleotide in the third exon which was found to be mutated in the ID patient ¹⁶. We
 223 designed a targeting vector containing two homology arms and a third segment
 224 containing the modification to be inserted in the mouse genome. In order to allow
 225 genotyping of the animals, a random sequence was inserted upstream the third exon
 226 (green sequence; Fig. 3a). Confirmation of the mutation was performed by Sanger
 227 sequencing (Fig. 3b). Heterozygous and homozygous KI mice were viable, did not
 228 display gross abnormalities, and did not show spontaneous seizures. To determine
 229 whether expression of the stargazin V143L variant affects gross brain morphology, we
 230 performed Nissl staining in brain coronal slices and compared sections from WT and
 231 homozygous stargazin V143L KI (KI^{VL/VL}) mice. As shown in Figure 3c, no apparent
 232 macroscopic defects were visible in the brain of stargazin KI^{VL/VL} animals when compared
 233 with WT littermates, suggesting that overall brain morphology is not affected by
 234 expression of the stargazin V143L mutation. Moreover, the structural organization of the
 235 hippocampus and the cortical lamination were preserved (Figs. 3c and S5b,c).

236 To assess whether the V143L stargazin mutation affects stargazin protein levels and
 237 distribution across the brain, we performed immunolabeling of stargazin in brain coronal
 238 and sagittal slices from WT and stargazin V143L KI mice. Stargazin is broadly expressed
 239 throughout the mouse brain with high expression levels in the cerebral cortex,
 240 hippocampus, and cerebellum ⁴. Within the hippocampus, stargazin immunoreactivity
 241 was more intense in the *stratum oriens* of the CA1, CA2 and C3 regions, the *stratum*
 242 *lacunosum moleculare* of the CA1 and CA2 regions, and particularly in the *subiculum*
 243 (Fig. S5a,b). Stargazin immunoreactivity was similar in all genotypes (Fig. 3d and S5b,c),
 244 indicating that the expression of the ID-associated form of stargazin does not affect the
 245 protein brain-wide distribution and total expression levels. This was also confirmed by
 246 western blot analyses, using total lysates from the whole brain, cortex and hippocampus
 247 (Fig. 3e, Fig. S5d,e). The expression levels of stargazin and other TARPs were also

assessed by qPCR and no changes were detected in samples from the cortex and hippocampus of KI mice, compared to WT littermates (Fig. S5f).

Since the V143L stargazin mutation was found in an ID patient¹⁶, we asked whether stargazin V143L KI mice display alterations in motor function, anxiety-like behavior, cognitive and/or social performance that correlate with ID-like symptomatology. We began by assessing motor behavior in the open field test (Fig. S6a) and found that, whereas male stargazin KI^{+VL} and KI^{VL/VL} mice showed comparable distance travelled and instant speed to WT male mice (Fig. S6c,e), female stargazin KI^{VL/VL} mice travelled longer distances, and stargazin KI^{+VL} female mice showed higher instant speed than WT female mice (Fig. S6b,d), suggesting hyperactivity in female stargazin V143L KI animals. However, stargazin V143L KI mice did not display anxiety-like behaviors either in the open field (Fig. S6f) or in the elevated plus maze (Fig. S6g,h) tests, nor did they show depressive-like behavior in the forced swimming test (Fig. S6i,j). In an object displacement test for spatial memory evaluation, while WT animals preferred to spend time engaging with the displaced object, neither stargazin KI^{+VL} nor KI^{VL/VL} mice showed this preference, and stargazin KI^{VL/VL} mice spent significantly less time exploring the object that was moved when compared to WT animals (Fig. 4a,b). Furthermore, male stargazin V143L KI animals failed to alternate above chance level in the T-maze spontaneous alternation test (Fig. S6k,l). In the contextual fear conditioning test for associative memory, stargazin KI^{VL/VL} mice presented less freezing behavior than WT animals (Fig. 4c,d). These observations suggest that the V143L mutation in stargazin elicits learning and memory impairments. Given the high expression of stargazin in the cerebellum (Tomita et al 2003), we assessed motor learning of stargazin V143L KI animals in the rotarod test (Fig. 4e-g). No significant motor abnormalities were displayed by mutant mice in the rotarod test (Fig. 4f), but whereas WT and stargazin KI^{+VL} mice improved their performance the second day they were placed in the apparatus, stargazin KI^{VL/VL} mice failed to do so, suggesting an impairment in motor learning (Fig. 4g).

275 Typically, ID patients display deficits in several social skills, including the will/ability to
276 socially engage with other people. To determine whether stargazin V143L KI mice
277 display social interaction deficits, we tested these animals in the three-chamber test.
278 Stargazin V143L KI mice showed preference for a conspecific (Stranger 1) over an empty
279 cage (E), similarly to WT mice (Fig. 4h-j). However, in the presence of a novel social
280 partner (Stranger 2), contrarily to WT and stargazin KI^{+VL} mice, stargazin KI^{VL/VL} mice did
281 not prefer to interact with the unfamiliar animal (Fig. 4h,k,l). This result suggests a
282 possible deficit in social recognition and/or alterations in the motivation for social novelty.
283 The innate social behavior of nest building was not perturbed in stargazin V143L KI mice
284 (Fig. S6n,o). Together, our results show that the ID-associated mutation in stargazin
285 elicits cognitive and social deficits reminiscent of ID-like symptoms.

286

287 **Stargazin V143L mutant mice exhibit early hippocampal synaptic transmission** 288 **defects**

289 To assess whether the decrease in surface AMPA receptor levels observed *in vitro* in
290 neurons expressing stargazin V143L has an impact in glutamatergic transmission *in vivo*,
291 we performed whole-cell patch-clamp recordings in CA1 pyramidal neurons from acute
292 hippocampal slices of P15-P20 stargazin V143L KI mice, to measure AMPA receptor-
293 mediated miniature excitatory post-synaptic currents (mEPSCs). We found that the
294 frequency of mEPSCs events was significantly decreased in neurons from stargazin
295 KI^{+VL} and KI^{VL/VL} mice compared to WT littermates (Figs. 5a,c). Interestingly, no changes
296 in the amplitude of mEPSCs (Figs. 5a,b) or in the kinetics of these events (Fig. 5a) were
297 observed. These data indicate that the V143L mutation in stargazin does not impact
298 AMPAR gating, but affects synaptic transmission in the hippocampus.

299 We next investigated the consequences of the ID-associated stargazin mutation in
300 hippocampal functional connectivity and synaptic plasticity by recording field excitatory
301 post-synaptic potentials (fEPSPs) in CA1 while stimulating the Schaffer collateral fibers.

302 First, we tested the impact of the V143L stargazin mutation on the CA3-to-CA1 Schaffer
303 collateral synaptic transmission and did not find significant differences in input/output
304 curves (Fig. 5d). This suggests that the connectivity between CA3 pre- and CA1 post-
305 synaptic sites is preserved in the hippocampus of stargazin V143L KI animals.
306 Additionally, no significant alterations were found in the fiber volley amplitude between
307 genotypes, indicating that there are no gross presynaptic impairments in stargazin
308 V143L KI mice at these synapses (Fig. 5d). Indeed, when paired-pulse facilitation, a
309 short-term strengthening of synaptic transmission, was assessed no overt alterations
310 were observed (Fig. 5e,f), further supporting that the presynaptic function is intact in the
311 hippocampus of stargazin V143L KI mice. Finally, we induced LTP in acute hippocampal
312 slices using a theta burst stimulation protocol. Stargazin V143L KI mice showed normal
313 LTP at Schaffer collateral-CA1 synapses (Fig. 5g,h). Altogether, these data indicate that,
314 despite the decreased frequency of mEPSC events detected in CA1 pyramidal neurons
315 (Fig. 5a,c), synaptic connectivity and theta burst-induced long-term synaptic potentiation
316 in the Schaffer collateral-CA1 synapse are not severely impaired in stargazin V143L KI
317 mice.

318

319 **Stargazin V143L mutant mice have reduced mature spine density on basal** 320 **dendrites of CA1 hippocampal neurons**

321 Dendrites and spines are key neuronal structures in signal integration and transmission.
322 Changes in dendritic branch complexity and length, and spine density, volume and
323 shape have been described in the brains of patients with neuropsychiatric disorders
324 [reviewed in ³⁶]. To understand if the stargazin V143L mutation impacts neuronal
325 morphology, we performed Sholl analysis of CA1 pyramidal neurons of stargazin V143L
326 KI mice. This structural analysis allows the evaluation of alterations in dendritic
327 complexity based on the number of dendritic intersections at various distances from the
328 soma. For that, we intravenously injected AAV9.hSyn.GFP in the mice to achieve sparse,

329 Golgi-like, labelling of neurons and outline the morphology of dendrites and dendritic
330 spines (Fig. S7a,b). Our results show that the stargazin V143L mutation has no impact
331 on dendritic arbor complexity (Fig. S7c,d). Moreover, no statistically significant
332 differences were found in the total dendritic length of basal and apical dendrites (Fig.
333 S7e).

334 Next, we evaluated the effects of the stargazin V143L mutation on dendritic spine density
335 and morphology in the hippocampus of stargazin V143L KI mice. While no significant
336 differences in total dendritic spine density were observed, there was a significant
337 decrease in the density of mature spines, namely mushroom and stubby spines, on basal
338 dendrites of CA1 pyramidal neurons from stargazin KI^{+VL} and KI^{VL/VL} mice when
339 compared to WT littermates (Fig. 6a,b). Additionally, stargazin KI^{+VL} and KI^{VL/VL} mice
340 displayed increased density of branched spines and of immature spines (thin and
341 filopodia) on basal dendrites (Fig. 6a,b). In contrast, no changes in spine density or
342 morphology were found on apical dendrites of CA1 pyramidal neurons of stargazin
343 V143L KI mice (Fig. 6c,d). Overall, there was a significant decrease in the percentage of
344 mature spines on basal dendrites of stargazin V143L KI mice neurons, whereas no
345 changes were observed on the morphology of spines on apical dendrites (Fig. 6e).
346 Interestingly, in the CA1 region stargazin was more expressed in the *stratum oriens*,
347 where the basal dendrites are located, when compared to the *stratum radiatum*, where
348 apical dendrites are placed (Fig. S5a). This differential pattern of stargazin expression
349 within the CA1 region correlates with the pronounced effects in spine maturation
350 observed on basal dendrites. To conclude, these data show that the stargazin V143L
351 mutation specifically results in spine dysmorphogenesis on basal dendrites without
352 having a major role on the formation/elimination of dendritic spines.

353 To further explore the alterations in spine morphology, we performed ultrastructural
354 analysis of the post-synaptic density (PSD) in hippocampal spines from WT and
355 stargazin V143L KI mice using electron microscopy. Our analysis uncovered a significant

356 decrease in the length of PSDs from stargazin KI^{+VL} and KI^{VL/VL} mice (Fig. 6g,h,k), as
 357 well as an increase in the thickness of PSDs from stargazin KI^{VL/VL} mice when compared
 358 with WT littermates (Fig. 6g,i,l), highlighting potential alterations in post-synaptic
 359 structure and composition. In stargazin KI^{VL/VL} mice there was a slight but significant
 360 increase in the synaptic cleft width (Fig. 6j,m). Moreover, the total levels of PSD95 in the
 361 hippocampus of stargazin V143L KI mice were significantly reduced compared to WT
 362 littermates (Fig. 6f). PSD95 has an important role in silent synapse maturation³⁷ and
 363 PSDs with smaller size and decreased PSD95 content are less stable³⁸. The decreased
 364 PSD95 levels further support an impairment in spine maturation in the hippocampus of
 365 stargazin V143L KI mice. Since stargazin is also expressed in the cortex, we analyzed
 366 the effects of the stargazin V143L mutation in the ultrastructure of PSDs from this brain
 367 region as well (Fig. S8a-g). We also observed a significant decrease in the length of
 368 PSDs of stargazin KI^{VL/VL} mice (Fig. S8a,b,e). However, in contrast to what was observed
 369 in the hippocampus, there was a significant decrease in the thickness of PSDs from
 370 stargazin KI^{+VL} mice (Fig. S8a,c,f). No changes in the synaptic cleft width were observed
 371 in cortical PSDs (Fig. S8a,d,g) nor in the total levels of PSD95 (Fig. S8h) in the cortex of
 372 stargazin V143L KI mice.

373 Together, these data reveal that the stargazin V143L mutation leads to an increase in
 374 the density of spines with immature morphology and to ultrastructural changes in post-
 375 synaptic compartments, indicating a general spine immaturity state in certain
 376 hippocampal subregions of stargazin V143L KI mice. Combined with our functional
 377 characterization showing decreased frequency of mEPSC events in CA1 neurons from
 378 stargazin mutant mice, this strongly suggests that the stargazin V143L mutation perturbs
 379 spine maturation and diminishes functional synaptic contacts in specific hippocampal
 380 subcircuits.

381

382 **Stargazin phosphorylation and interaction with GluA1 are decreased in stargazin** 383 **V143L mutant mice**

384 In a final set of experiments, we sought to determine whether the dendritic spines
385 immaturity (Fig. 6a,b,e) and the decreased PSD length (Figs. 6h-m and S8a,b,e) found
386 in the brain of stargazin V143L KI animals are accompanied by altered composition of
387 the PSDs. We isolated PSDs from the cerebral cortex of WT, stargazin KI^{+VL} and KI^{VL/VL}
388 littermate mice (Fig. S8i) and quantified their content in stargazin, GluA1 and GluA2
389 AMPAR subunits, as well as PSD95 (Fig. 7a-e). Stargazin expression was decreased in
390 the PSDs of stargazin KI^{+VL} and KI^{VL/VL} mice compared to WT mice (Fig. 7a, despite not
391 significantly changed total expression levels of stargazin in mutant mice - Fig. 3e), in
392 agreement with increased cell surface mobility and decreased synaptic residence of
393 stargazin V143L compared to the WT protein (Fig. 2a-f). Heterozygous stargazin V143L
394 mice showed decreased levels of GluA1, GluA2 and PSD95 at the PSD, which were not
395 significantly changed in homozygous stargazin KI^{VL/VL} mice (Fig. 7a, c-e). These
396 observations suggest that the V143L mutation in stargazin impairs its expression at the
397 synapse, which interferes with the synaptic content of AMPAR subunits. However, in
398 homozygous mutant mice other TARPs may preferentially bind to AMPAR subunits and
399 partially compensate for mutant stargazin in AMPAR synaptic trafficking. Indeed, and in
400 agreement with our molecular dynamics analyses (Fig. 1e), immunoprecipitation of
401 stargazin V143L from the cerebral cortex of stargazin KI^{VL/VL} mice showed decreased co-
402 immunoprecipitation of GluA1, compared with stargazin immunoprecipitated from the
403 cortex of WT littermate mice (Fig. 7f,g), indicating that the V143L mutation in stargazin
404 impairs its interaction with AMPAR subunits *in vivo*.

405 The function of stargazin is regulated by the phosphorylation of serine residues in the
406 cytoplasmic C-terminal tail of the protein¹², and these phosphorylation events regulate
407 stargazin interaction with membrane lipids³⁹, its binding to PSD95^{9,40}, and the diffusional
408 trapping of AMPARs at synaptic sites³³. The migration pattern of stargazin in denaturing

409 SDS-PAGE conditions correlates with the phosphorylation state of the protein, with
 410 phosphorylated stargazin showing slower migration in SDS-PAGE ^{11,12}. We noticed that,
 411 in PSDs isolated from the cortex of stargazin KI^{VL/VL} mice, stargazin showed faster
 412 migration compared to PSDs isolated from WT mice, whereas an intermediate migration
 413 pattern was detected in PSD isolated from heterozygous stargazin V143L mice (Fig.
 414 7h,i). To test for altered phosphorylation of mutant stargazin, we treated cortical extracts
 415 with λ-phosphatase before PSD purification and found that stargazin bands in PSDs
 416 isolated from the cortex of WT or heterozygous stargazin KI^{+/VL} mice shifted to a lower
 417 apparent molecular weight, putatively corresponding to the unphosphorylated form of the
 418 protein ^{11,12} and coincident with the stargazin band in PSDs isolated from untreated
 419 cortical extracts from stargazin KI^{VL/VL} mice (Figs. 7j-l). In fact, the gel mobility of the
 420 stargazin band in PSDs isolated from stargazin KI^{VL/VL} mice was unchanged by λ-
 421 phosphatase treatment (Figs. 7j-l), indicating that the protein is in a dephosphorylated
 422 form. These findings are consistent with decreased phosphorylation of V143L stargazin.
 423

424 DISCUSSION

425 In this study, we employed molecular dynamics analyses, *in vitro* and *in vivo* models to
 426 study how an ID-associated mutation in the third transmembrane domain of stargazin
 427 impacts the AMPAR:stargazin complex, hippocampal synaptic architecture, synapse
 428 function and behavior. Our data suggest that the V143L mutation in stargazin critically
 429 affects stargazin interaction with the AMPAR complex, leads to decreased stargazin
 430 phosphorylation, decreases AMPAR-mediated synaptic transmission and contributes to
 431 spine immaturity in CA1 hippocampal neurons. A striking aspect of our study is that it
 432 reveals not only the pathogenic effect of a mutant form of stargazin associated with
 433 disease, but also unveils critical roles for stargazin in regulating synapse structure and
 434 function in the hippocampus and in shaping cognitive and social behavior.

435 Structural analyses highlight that the main interface between AMPAR:stargazin is in the
436 TMD of the complex, where the ECD of stargazin acts as a scaffold on the receptor. This
437 interaction is mainly mediated by TMD3 and TMD4 from stargazin, M1 and M2 from *Main*
438 *GluA*, and M4 from *Auxiliary GluA*. Our analysis showed a positively correlated motion
439 between these substructures (Fig. 1e), which presented lower Δ SASA values, indicating
440 their higher contribution to the overall interface. The stargazin V143L mutation hinders
441 the correlated motion between TMD regions of stargazin and GluA, especially at M4 of
442 *Auxiliary GluA*. Furthermore, Δ SASA values for these substructures are higher in the
443 systems containing mutated stargazin. X site shows greater differences between WT
444 and mutant stargazin, suggesting that the stargazin V143L mutation especially weakens
445 AMPAR:stargazin interaction at the X site. In agreement with a weakening effect of the
446 V143L mutation on the interaction between stargazin and AMPAR, we found a
447 decreased co-immunoprecipitation of GluA1 with stargazin V143L (in cortical brain
448 lysates from stargazin KI^{VL/VL} mice) compared to WT stargazin (Fig. 7f,g). Furthermore,
449 we observed decreased trafficking of AMPAR to the synapse upon deletion of stargazin,
450 which was not rescued upon expression of the ID-associated variant of stargazin in
451 cortical neurons (Fig. 2g-l).

452 To date, the physiological roles of TARPs have been studied using knock-out mice for
453 the different TARPs, alone or in combination [reviewed in ²]. These analyses have
454 provided crucial insight into partially overlapping although non-redundant functions for
455 different TARPs, but are hindered by possible compensatory effects that may arise in
456 the absence of the endogenous proteins. Examining knock-in mouse models expressing
457 mutant forms of stargazin associated with disease has the double advantage of informing
458 on the endogenous role of stargazin, by analyzing the effects of loss of function mutant
459 variants which are still expressed, and on possible pathogenic mechanisms elicited by
460 human stargazin mutations. In this study, we have found that the V143L mutation in
461 stargazin triggers a striking decrease in the frequency of mEPSCs in hippocampal CA1

pyramidal neurons (Fig. 5a-c), and leads to a decrease in spine maturity in CA1 basal dendrites (Fig. 6a, b,e), and to ultrastructural alterations in the post-synaptic compartment, in particular a significant reduction of the PSD length (Fig. 6g-m). These observations suggest that despite the expression of multiple other TARP members in the hippocampus, including $\gamma 3$ and high enrichment in $\gamma 8$ (Tomita et al 2003), stargazin is required for normal spine and PSD development and for maintaining a full complement of functional synapses. Our results are in line with experiments using *stargazer*/ $\gamma 8$ -knock-out mice, which showed that AMPAR-mediated transmission in CA1 pyramidal neurons is further reduced, compared to the reduction observed in $\gamma 8$ -knock-out mice⁴¹, despite the fact that CA1 pyramidal neurons from *stargazer* mice did not show alterations in the ratio of AMPA to NMDA EPSC amplitudes⁴². The synergistic reduction in AMPAR-mediated transmission in the *stargazer*/ $\gamma 8$ double knock-out mice implies some degree of functional redundancy for the two TARPs. If mutated stargazin is expressed, its incorporation in AMPAR complexes, even if less efficient than WT stargazin, will thus exert pathogenic effects, as suggested by the reduction in the frequency of mEPSCs and in spine maturation that we observed in stargazin V143L mice. These results are also in agreement with electron microscopy data showing that at Schaffer collateral/commissural synapses in the CA1 hippocampal region the presence of stargazin correlates with higher density of AMPAR expression⁴³ and thus presumably with the presence of a higher number of functional synapses.

Our data show a specific effect of the stargazin V143L variant in spine maturation in basal dendrites in CA1 neurons, which was not observed in apical dendrites (Figs. 6a-e). Indeed, despite the significant change in the frequency of mEPSC in CA1 neurons in stargazin V143L mice (Figs. 5a-c), we found no changes in field EPSC slope (Fig. 5d) or in LTP (Fig. 5g,h) in Schaffer collateral-CA1 synapses recorded in the *stratum radiatum*, which are located in the apical dendrites of CA1 pyramidal neurons. These observations indicate that stargazin has a specific role in maintaining spine structure in CA1 basal

dendrites, which is in agreement with the higher expression levels of stargazin in the hippocampal *stratum oriens*, compared with the *stratum radiatum* (Fig. S5a). Altogether, our data suggest that, besides the well-described brain region- and cell type-specific roles of TARPs, there may be subcellular-specific roles that are determined by the subcellular distribution pattern of different TARPs.

The V143L variant of stargazin was found to be dephosphorylated in cortical PSDs isolated from homozygous stargazin V143L KI mice, compared to WT PSDs (Fig. 7h-l). Phosphorylation of stargazin in its C-terminal region disrupts electrostatic interaction between the membrane and stargazin C-tail³⁹, promotes the extension of the C-tail into the cytoplasm and binding to PSD95⁴⁰, and triggers diffusional trapping of AMPARs at synaptic sites³³. Stargazin phosphorylation has been proposed to regulate Hebbian forms of synaptic plasticity¹² and to mediate experience-dependent plasticity and synaptic scaling^{10,11}. The lower level of phosphorylation of stargazin-V143L compared to the WT protein likely underlies its higher membrane diffusion rate at the membrane and its impaired capacity in supporting AMPAR synaptic traffic (Fig. 2). The low phosphorylation of stargazin V143L may also determine the sequestration of its C-terminal tail in the plasma membrane and thus impair it from undergoing liquid-liquid phase separation with PSD scaffold proteins⁹. Changes in hippocampal spine maturation and in the ultrastructure of the hippocampal PSDs (Fig. 6) may thus be a consequence of defective stargazin V143L phosphorylation, and may be reflected in the decreased number of functional synapses detected in our mEPSC analyses in CA1 hippocampal neurons (Fig. 5a-c). While it is likely that the aberrant stargazin V143L phosphorylation contributes to the physiological effects observed, our MD analysis, which does not take into account post-translational modifications in stargazin, also suggests compromised function for the V143L stargazin variant.

In this study we found that the V143L mutation in stargazin in male and female stargazin KI^{VL/VL} mice leads to altered spatial memory (Fig. 4a,b), assessed using the object

516 displacement test, as well as perturbed associative memory in the contextual fear
517 conditioning test (Fig. 4c,d). These alterations in hippocampal-dependent cognitive
518 behavior are likely to be related to the changes in mEPSC frequency, in spine maturity
519 and in PSD ultrastructure that we identified in the hippocampus of these mice. We did
520 not detect changes in social interaction in the three chamber test in stargazin V143L
521 mice (Fig. 5i,j), but stargazin KI^{VL/VL} mice showed impairment in preference for social
522 novelty (Fig. 5k,l), suggestive of either a perturbation in social memory or a lack of
523 motivation for social novelty. Stargazin KI^{VL/VL} mice also displayed impaired motor
524 learning in the rotarod (Fig. 5g), pointing to possible functional and structural alterations
525 in the cerebellum caused by the stargazin V143L mutation. Given the elevated
526 expression of stargazin in the cerebellum ⁴ and its non-redundant functions in cerebellar
527 excitatory synapses in several cerebellum circuits ^{2,7,42}, future studies should examine
528 cerebellum circuit-specific dysfunction triggered by the ID-associated stargazin mutation.
529 The cognitive and social behavioral dysfunctions displayed by stargazin V143L mice
530 most likely arise from alterations in a combination of brain circuits, depending on the
531 stargazin expression pattern and its synaptic roles in different cell types. Together, our
532 data provide the first evidence for the causal implication of stargazin in the pathogenesis
533 of neurodevelopmental disorders.

534 **METHODS**

535 **Modeling the three-dimensional protein structure**

536 The three-dimensional (3D) structure of stargazin was constructed by homology
 537 modelling using the MODELLER package ⁴⁴, the target sequence retrieved from UniProt
 538 [⁴⁵, Q9Y698] and two templates: GluA2:stargazin complex [PDB-ID: 6DLZ ²⁸; electron
 539 microscopy with 3.9 Å resolution; Human Organism; 99.5% sequence similarity]. The
 540 best one hundred models from MODELLER ⁴⁴ were evaluated by DOPE score, z-score
 541 ^{46,47}, LGscore and MaxSub ⁴⁸. The final model loops were further optimized. Due to the
 542 lack of a well-defined secondary structure with subsequent high conformational
 543 heterogeneity, the C-terminal of this protein, located at the intracellular level, was
 544 removed from the final model. The V143L stargazin mutation was built using the
 545 mutagenesis tool of PyMOL, creating the ID model. The 3D structure of GluA2 (Ligand-
 546 binding domain – LBD - and transmembrane domain – TMD) was also constructed using
 547 the MODELLER package ⁴⁴ and the subunit of AMPAR as the template (PDB-ID: 6DLZ),
 548 with the sequence P42262 from UniProt. The final model was selected using the previous
 549 criteria and the complexes AMPAR:stargazin (WT and V143L variant) were obtained by
 550 the superimposition of the stargazin and AMPAR models with 6DLZ structure. The final
 551 model 3D structure is illustrated in Figure 1b.

552 **Molecular dynamics simulations**

553 Molecular Dynamics (MD) simulations of AMPAR:stargazin WT and mutated form
 554 (V143L variant) were performed using GROMACS 2018.4 ⁴⁹ and the CHARMM36 force
 555 field ⁵⁰. The complex orientation in the membrane was obtained through the oriented
 556 crystal of GluA2:stargazin complex (PDB-ID: 6DLZ). Systems were built using
 557 CHARMM-GUI ^{51,52} membrane builder with a bilayer membrane of POPC:Cholesterol
 558 (9:1 ratio) to replicate the physiological environment. Each complex was solvated by a

559 TIP3 water box and 0.15 M of NaCl. The final WT and mutated systems were constituted
560 by 518.000 and 521.000 atoms, respectively.

561 The systems were subjected to an initial minimization to remove bad contacts using the
562 steepest descent algorithm. Subsequently, they were heated using the Berendsen-
563 thermostat at 310 K in the NVT ensemble over 7 ns, followed by an NPT ensemble of 20
564 ns with a semi-isotropic pressure coupling algorithm ⁵³, which is used to keep the
565 pressure constant of one bar. Long-range electrostatic interactions were treated by the
566 fast smooth Particle-Mesh Ewald method ⁵⁴. All bonds, involving hydrogen atoms within
567 protein and lipid molecules were constrained using the linear constraint solver (LINCS)
568 algorithm ⁵⁵. Additionally, a cut-off distance of 12 Å was attributed to Coulombic and van
569 der Waals interactions. Three independent replicas were run for each system during 0.5
570 µs, of which the first 0.15 µs of equilibration were left out of the further analysis.

571 Root mean square deviations (RMSD) calculations were performed using the Cα atoms
572 by GROMACS package ⁴⁴. The cross-correlation analysis (CCA), which tracks the
573 movements of two or more sets of time series data relative to one another, was
574 calculated by Bio3D R package ⁵⁶ for residue-level dynamic analysis using the Cα
575 trajectory. CCA analysis provides atomistic detail about the dynamic nature of proteins,
576 and in particular allows the differentiation between regions that exhibit correlated or
577 anticorrelated motions with others, in the same or in the opposite direction, respectively
578 ⁵⁷. The solvent-accessible surface area (SASA) analysis for each residue was performed
579 using GROMACS package ⁴⁹. These analyses were performed for the bound and
580 unbound systems, and ΔSASA by residue was calculated as $SASA_{AMPAR-STG} - (SASA_{GluA2} + SASA_{STG})$. ΔSASA values, summed by substructure, provide another quantitative
581 + SASA_{STG}). ΔSASA values, summed by substructure, provide another quantitative
582 measure of conformational change upon protein coupling ⁵⁸.

583

584 **Primary cortical neurons**

585 Primary cultures of rat cortical neurons were prepared from the cortices of E17 Wistar
586 rat embryos. Briefly after dissociation, the cortices were incubated with trypsin (0.06%,
587 10 min, 37°C, GIBCO Invitrogen) in Ca²⁺- and Mg²⁺-free HBSS (5.36 mM KCl, 0.44 mM
588 KH₂PO₄, 137 mM NaCl, 4.16 mM NaHCO₃, 0.34 mM Na₂HPO₄·2H₂O, 5 mM glucose,
589 1 mM sodium pyruvate, 10 mM HEPES and 0.001% phenol red), washed 6 times with
590 HBSS and then mechanically dissociated. After counted, the cells were plated, at a low
591 density (0.3x10⁶ cells per 60 mm culture dish), in neuronal plating medium (MEM
592 supplemented with 10% horse serum, 0.6% glucose and 1 mM pyruvic acid) in five poly-
593 D-lysine (0.1 mg/ml) coated coverslips (18 mm). The medium was replaced, after 2
594 hours, by Neurobasal medium supplemented with SM1 (StemCell Technologies), 0.5
595 mM glutamine and 0.12 mg/ml gentamicin. Neurons grew facing a confluent feeder layer
596 of astroglial cells but were kept apart from the glial cells by wax dots placed on the
597 coverslips⁵⁹. The cultures were treated with 5 µM cytosine arabinoside, two days after
598 plating, to prevent the overgrowth of glial cells and were maintained in an incubator with
599 5% CO₂, at 37°C. Conditioned medium was partially replaced by fresh, SM1
600 supplemented neurobasal medium every 3 days. Primary cortical cultures were used for
601 imaging.

602 **Transfection of cortical neurons**

603 Neurons were transfected using a calcium phosphate-mediated transfection protocol⁶⁰.
604 A CaCl₂ solution (2.5 M in 10 mM HEPES) was added, dropwise, to the diluted DNA.
605 This solution was then added to the equivalent volume of HEPES-buffered transfection
606 solution (274 mM NaCl, 10 mM KCl, 1.4 mM Na₂HPO₄, 11mM dextrose and 42 mM
607 HEPES, pH 7.2). The DNA precipitates were added, dropwise, to the coverslips in
608 conditioned medium and 2 mM of kynurenic acid. The cultures were incubated for 2 h at
609 37°C and 5% CO₂. The DNA precipitates were dissociated by incubating the cells with

610 acidified medium, for 15 minutes at 37°C and 5% CO₂. Coverslips were then transferred
611 to the original astroglial-containing dish.

612 **Immunocytochemistry and imaging**

613 In order to stain surface proteins, live cells were incubated with anti-GluA (MAB2263;
614 Millipore) primary antibody diluted in conditioned medium for 10 minutes and fixed for 15
615 min in 4% sucrose/ 4% paraformaldehyde in PBS at room temperature. Following 3
616 washes with PBS, the cells were incubated with the secondary antibody (Molecular
617 Probes) diluted in 3% BSA, in PBS, for 45 min, 37°C. After 6 washes with PBS, cells
618 were permeabilized for 5 min with 0,25% Triton X-100, in PBS at 4°C. Unspecific staining
619 was blocked by incubation with 10% (w/v) BSA in PBS for 30 min, at 37°C. In order to
620 label PSD95 (MA1-045; Thermo Scientific) and MAP2 (ab5392; Abcam), neurons were
621 incubated with the primary antibodies diluted in 3% BSA in PBS for 2h at 37°C or
622 overnight at 4°C. Before and after incubating with the secondary antibodies, also diluted
623 in 3% BSA in PBS, for 45 min, 37°C, cells were washed 6 times with PBS. Coverslips
624 were mounted in DAKO fluorescent mounting medium. The imaging was performed
625 using a Zeiss Axiovert 200 M microscope and a 63X (NA1.4) oil objective. Blind-to-
626 condition quantification was performed in ImageJ analysis software, with a macro that
627 automatized quantification steps. The region of interest (ROI) was chosen randomly, by
628 using MAP2 and/or GFP staining to confirm that the selected dendrite was from a
629 transfected neuron. The threshold was defined to include detectable clusters and the
630 signal intensity of the particles of the selected area was analyzed. Synaptic puncta were
631 defined by their colocalization with PSD95.

632

633 **Quantum dots labeling, imaging and analysis**

634 Low-density 12 days *in vitro* (DIV) cells were co-transfected with plasmids encoding
635 Homer-GFP, for synapse identification, and HA-tagged WT stargazin or the V143L

636 stargazin variant. At DIV 14, cells were incubated for 10 min at 37°C with anti-HA
637 antibody (3F10; Roche) (1:3000) diluted in conditioned medium. After one washing step,
638 anti-rat IgG conjugated QD655 (diluted 1:10 in PBS) was diluted in conditioned medium
639 with BSA 2% (1/2000) and added to cells for 5 min at 37°C. All washes were performed
640 in ECS containing NaCl 145mM, KCl 5mM, Glucose 10mM, Hepes 10mM, CaCl₂ 2 mM
641 and MgCl₂ 2mM, supplemented with BSA 2% at 37°C. Neurons were mounted in an
642 open chamber (K.F. Technology SRL) and imaged in ECS. Single-particle tracking was
643 performed as in (Opazo et al 2010). Cells were imaged at 37°C on an inverted
644 microscope (Axio Observer Z1, Carl Zeiss) equipped with a Plan Aplanachromat 63X-1.4
645 numerical aperture oil objective. Homer1C-GFP signal was detected by using an HXP
646 fluorescence lamp (For QDs: excitation filter 425/50 and emission filters 655/30,
647 Chroma). Fluorescent images from QDs were obtained with an integration time of 50 ms
648 with up to 600 consecutive frames. Signals were recorded with a digital CMOS camera
649 (ORCA Flash 4.0, Hamamatsu). The tracking of single QDs was performed using the
650 Metamorph and Matlab (Mathworks Inc., Natick, USA) software tools. Due to random
651 blinking, the trajectories were not continuously tracked, instead, when the positions
652 before and after the dark period were compatible with borders set for maximal position
653 changes between consecutive frames and blinking rates, the subtrajectories of the same
654 molecule were reconnected. MSD curves were calculated for reconnected trajectories of
655 at least 20 frames. The QDs were considered synaptic if colocalized with Homer-1c
656 dendritic clusters for at least five frames. Diffusion coefficients were calculated by a linear
657 fit of the first 4–8 points of the mean square displacement (MSD) plots versus time
658 depending on the length of the trajectory within a certain compartment. The resolution
659 limit for diffusion was 0.0075 $\mu\text{m}^2/\text{s}$ as determined by⁶¹, whereas the resolution precision
660 was ~40 nm.

661

662 **Animal generation and maintenance**

663 Stargazin V143L KI mice were generated by inserting a single nucleotide mutation in the
 664 third exon of the *Cacng2* gene. The targeting vector was introduced through homologous
 665 recombination in R1 cells, as described previously⁶². Mice were viable and born at the
 666 expected Mendelian ratio. Genotyping was performed by PCR from mouse ear or tail
 667 DNA using a forward primer for the WT allele (AAGGGACCCTCCGTCCTCTC), a
 668 forward primer for the KI allele (GGGCCCGGTGCAATACACGC) and a reverse primer
 669 for both the reactions (CATCGGGCATGGATCCTCAGTTC). Mice were maintained at
 670 22°C and 60% humidity under a 12h light/dark cycle. Food and water *ad libitum* were
 671 provided. During this study, both male and female animals were used. The imaging,
 672 biochemical and behavioral analyses were performed in mice with 8 to 10 weeks and
 673 electrophysiology recordings were performed in 15-20 days-old animals. All the
 674 procedures involving animals were performed according to the guidelines established by
 675 the European Union Directive 2010/63/EU and the experiments were previously
 676 approved by the institutional animal welfare body (ORBEA) and the national competent
 677 authority (DGAV).

678 **Nissl Staining**

679 Eight-week old mice were anesthetized with isoflurane and perfused with ice cold PBS
 680 followed by 4% paraformaldehyde in PBS. Whole brains were kept in 4%
 681 paraformaldehyde in PBS overnight and then transferred to a 30% sucrose in PBS
 682 solution for at least 24 hours. Brains were sliced in the cryostat (Thermo Cryostar NX50,
 683 Thermo Fisher Scientific, USA) to obtain 50 µm coronal slices which were mounted in
 684 gelatin-coated slides. The slides were briefly washed with water and then submersed in
 685 a cresyl violet solution, for 5 minutes. After 2 washes with water, the slices were
 686 decolorized with 100% ethanol for 2 minutes and incubated for 2 minutes in xylene before
 687 mounting with Permount mounting medium (Fisher scientific). Brain slices were digitized

688 using a Zeiss Axio Scan.Z1 slide scanner (Carl Zeiss, Germany) equipped with a Plan
689 Apochromat 20X-0.8 numerical aperture air objective.

690 **Immunohistochemistry**

691 For stargazin immunofluorescence staining, 50 μ m coronal and sagittal brain slices were
692 prepared as described above. Free-floating sections were rinsed 3 times in PBS for 10
693 minutes and then permeabilized and blocked for 1 hour at room temperature with 0.25%
694 Triton X-100 and 5% goat serum in PBS. After that, slices were incubated overnight at
695 room temperature with the primary antibody (AB_2571844, Frontier Institute Co., Japan)
696 diluted 1:200 in 0.25% Triton X-100 and 2% goat serum in PBS, followed by 3 washes
697 with 0.25% Triton X-100 in PBS. Sections were incubated with the secondary antibody
698 (anti-rabbit Alexa Fluor 568, Molecular Probes, USA) diluted 1:500 in 0.25% Triton X-
699 100 and 2% goat serum in PBS, at room temperature for 2 hours. Nuclei were visualized
700 by staining with 1 μ g/mL Hoechst 33342 in PBS for 5 minutes at room temperature.
701 Lastly, after 3 washes of 10 minutes in PBS, the sections were mounted in gelatinized
702 slides using Dako mounting medium (Glostrup, Denmark). Images were acquired on a
703 Carl Zeiss Axio Imager Z2 upright widefield microscope (Carl Zeiss, Germany) using a
704 Plan-Apochromat 20x air objective (NA 0.8) or in an LSM 710 Confocal microscope
705 (Zeiss, Germany) with a Plan Apochromat 63x (NA 1.4) oil objective.

706 **Behavior analyses**

707 ***Object displacement test***

708 The ODT was performed in a 40x40 cm open field arena. The test consisted of five trials.
709 In the first trial the animals acclimatized to the empty arena for 6 minutes. In the three
710 following trials, the animals were allowed to explore, for 6 minutes, two different objects
711 located in a fixed position. In the fifth trial, conducted 24 hours later, one of the objects
712 was displaced and the time spent exploring the non-displaced and the displaced object
713 was evaluated.

714 Contextual fear conditioning test

715 The contextual fear conditioning test was performed in an electrified wire-bottom 20x20
716 cm cage. On the first day, the animal was placed for 2 minutes in the cage before
717 receiving a 2s-long foot shock of 0.5 mA. After 30 seconds, a second foot shock with the
718 same magnitude and duration was administered, another 30 seconds later the animal
719 was removed from the cage. After 24h, the animal was placed in the same cage and it
720 was recorded for 3 minutes. The time spent in freezing behavior was scored using the
721 Observer XT 12 software (Noldus, Netherlands).

722 Rotarod test

723 Motor function and learning was evaluated using the accelerated rotarod (Med
724 Associates), 4 to 40 rpm in 5 min. The time withstood in the rotating beam in three
725 successive trials in a single day, for 2 days, was evaluated. An improvement in the
726 performance in the second day was considered motor learning.

727 The three-chamber test

728 The three-chamber test was evaluated in a tripartite arena (Stoelting). The test was split
729 in three epochs. In the first part, the animal was allowed to freely explore the three
730 chambers of the arena for 20 minutes. In the second part the animal was allowed to
731 voluntarily interact with an empty gridded recipient or with a similar recipient containing
732 a stranger animal, for 10 minutes. The preference index for social behavior (S1:E) was
733 determined as follows: $\frac{\text{Sniffing time}(\text{Stranger 1}) - \text{Sniffing time}(\text{Empty cage})}{\text{Sniffing time}(\text{Stranger 1}) + \text{Sniffing time}(\text{Empty cage})} \times 100$. In the third
734 part of the trial, which also lasted 10 minutes, a second stranger was placed in the
735 previously empty recipient. The preference index for social novelty (S2:S1) was
736 determined as follows: $\frac{\text{Sniffing time}(\text{Strange 2}) - \text{Sniffing time}(\text{Stranger 1})}{\text{Sniffing time}(\text{Stranger 2}) + \text{Sniffing time}(\text{Stranger 1})} \times 100$. The time
737 spent in close proximity with the gridded recipients was evaluated using the Observer
738 XT 12 software (Noldus, The Netherlands).

739

740 **Slice preparation and electrophysiological recordings**

741 WT and stargazin V143L KI mice littermates (P15-P20) were deeply anesthetized with
 742 isoflurane and transcardially perfused with ice-cold sucrose cutting solution (212.7 mM
 743 sucrose, 2.6 mM KCl, 1.23 mM NaH₂PO₄, 26 mM NaHCO₃, 10 mM glucose, 3 mM MgCl₂,
 744 1mM CaCl₂, pH 7.4, 300–320 mOsm) oxygenized with carbogen (95% O₂ and 5% CO₂).
 745 The brain was quickly removed and immersed in oxygenated ice-cold sucrose cutting
 746 solution. 300 µm acute hippocampal sagittal slices were prepared using a vibratome
 747 (Leica VT1200s, Leica Microsystems, USA). The slices were collected and transferred
 748 to a submersion holding chamber with artificial cerebrospinal fluid (aCSF) continuously
 749 oxygenated with carbogen, at 32°C, for 30 minutes. After that, slices were allowed to
 750 further recover for 1 hour at room temperature, in oxygenated aCSF, before recording.
 751 aCSF composition (mM) for whole-cell patch-clamp recordings: 125.1 NaCl, 2.5 KCl,
 752 1.1 NaH₂PO₄, 25 NaHCO₃, 25.0 glucose, 0.5 MgSO₄, 2 CaCl₂, pH 7.4, 300–310 mOsm.
 753 aCSF composition (mM) for field recordings: 130.9 NaCl, 2.5 KCl, 1.1 NaH₂PO₄, 24.0
 754 NaHCO₃, 12.5 glucose, 0.5 MgSO₄, 2 CaCl₂, pH 7.4, 300–310 mOsm.

755 CA1 pyramidal neurons were visualized under infrared-differential interference contrast
 756 (IR-DIC) microscopy using an upright microscope (Axio Examiner.D1, Zeiss, Germany).
 757 Whole-cell voltage-clamp recordings were performed at a holding potential of -80 mV
 758 using a Multiclamp 700B amplifier, digitized at 20 kHz with Digidata 1550A (Molecular
 759 Devices Corporation), and acquired using Clampfit 10.7 software (Axon Instruments).
 760 Slices were kept in a recording chamber perfused with oxygenated aCSF (2–3 mL/min),
 761 at 30°C, supplemented with 1 µM TTX, 100 µM picrotoxin and 50 µM D-APV, to isolate
 762 AMPAR-mediated mEPSC. Borosilicate glass recording pipettes (3–5 MΩ) were filled
 763 with a Cs-based solution (115.0 mM CsMeSO₃, 20.0 mM CsCl, 2.5 mM MgCl₂, 10.0 mM
 764 HEPES, 0.6 mM EGTA, 10 mM Na-phosphocreatine, 4 mM ATP sodium salt, 0.4 mM
 765 GTP sodium salt, pH 7.3, 295–300 mOsm). Data were filtered at 2 kHz. Cells were
 766 discarded if Ra was higher than 25 MΩ or if holding current or Ra changed more than

767 20%. Data were analysed using Clampfit software (Axon Instruments) using a template
768 search method to detect events. Experiments and analysis were done blind to the
769 genotype.

770 fEPSPs were evoked by stimulating the Schaffer collaterals at 0.05 Hz using a bipolar
771 electrode (100 μ s stimulus; Bowdoin, ME, USA) connected to a stimulator Digitimer
772 model DS3 (Digitimer, UK) and recorded in CA1 *stratum radiatum*. Recordings were
773 performed at 25°C in a recording chamber constantly perfused with oxygenated aCSF
774 (2–3 mL/min). The recording pipette was filled with aCSF (2-4 M Ω). An input-output
775 curve, starting at 20 μ A with 10 μ A increments, was performed and the stimulation
776 intensity was set to elicit 40-50% of the maximal response. Only slices displaying a stable
777 signal response over a period of 10 minutes were used. Short-term synaptic plasticity
778 was assessed by measuring paired-pulse facilitation (PPF) using a standard protocol, as
779 previously described⁶³. LTP was induced by theta-burst stimulation (TBS; 10 bursts of
780 4 stimuli at 100 Hz with a burst frequency of 5 Hz)⁶⁴. A baseline was recorded in the
781 current-clamp mode with a single stimulation at 0.05 Hz (100 μ s stimulus) for 15 minutes
782 immediately before TBS. Changes in fEPSPs were recorded at 0.05 Hz for 60 minutes
783 after TBS. Recordings were filtered at 0.1 Hz-1 kHz and digitized at 10 kHz. For each
784 data point three individual traces were averaged. Fiber volley amplitude and synaptic
785 response slopes were analysed using Clampfit software.

786 **Labelling, detection and morphological classification of dendritic spines**

787 To achieve sparse labelling of neurons in the hippocampus, we performed tail-vein
788 injections in 4-week-old animals, with 5 μ L of AAV9.Syn.eGFP.WPRE.bGH at a titer of
789 8.88×10^{12} (Penn Vector Core, University of Pennsylvania, PA) diluted in sterile PBS to a
790 final volume of 100 μ L. Four weeks post-injection, animals were sacrificed and the brains
791 were collected and processed for neuronal imaging as already described. Brains were
792 sliced in the cryostat to obtain 100 μ m serial coronal slices and the GFP fluorescence

793 signal was enhanced by performing immunostaining against GFP. Sections were then
794 mounted in gelatinized slides using Vectashield with DAPI (Vector Laboratories, USA).
795 Images of secondary basal and apical dendrites from CA1 pyramidal neurons expressing
796 GFP were acquired in an LSM 710 Confocal microscope (Zeiss, Germany) with a Plan
797 Apochromat 63x (NA 1.4) oil objective. The dendritic segments imaged were randomly
798 selected from at least four different sections. Per each animal, eight basal and eight
799 apical dendritic segments, of approximately 20 μ m, from different cells were imaged. The
800 z-stack images were deconvolved using Huygens software (Scientific Volume Imaging,
801 Netherlands) and spines were visualized and identified using Imaris software (Bitplane,
802 Switzerland). Spines were manually categorized into five groups based on its
803 morphology: mushroom (defined neck and a large head), stubby (without a defined
804 neck), branched (cup-shaped; with a head protrusion; with multiple heads), thin (thin
805 neck and small head) and filopodia (without a defined head). Image acquisition and
806 analysis was performed by a blind-to-genotype observer.

807 **Electron microscopy**

808 Sample preparation and post-synaptic density parameter measurements were
809 performed as previously described in ⁶³. Eight-week-old mice were anesthetized with
810 isofluorane and transcardially perfused with ice-cold PBS followed by 4%
811 paraformaldehyde. Cortices and hippocampi were dissected, and small punches of
812 tissue were left overnight in PFA 4% and then transferred into a 2.5% glutaraldehyde
813 solution in 0.1 M sodium cacodylate buffer (pH 7.2), where they were kept at 4°C
814 overnight. The tissue was then rinsed in a cacodylate buffer and post-fixed with 1%
815 osmium tetroxide for 1 h. After rinsing in buffer and distilled water, 1% aqueous uranyl-
816 acetate was added to the tissues, in the dark, during 1 h for contrast enhancement.
817 Following rinsing in distilled water, samples were dehydrated in a graded acetone series
818 (70–100%) and then impregnated and included in Epoxy resin (Fluka Analytical).
819 Ultrathin sections (70 nm) were mounted on copper grids and observations were carried

820 out on a FEI-Tecnai G2 Spirit Bio Twin at 100kV. PSD measurements were performed
821 using ImageJ (NIH, Bethesda, Maryland) by a blind-to-genotype observer.

822 **Tissue lysates and post-synaptic density isolations**

823 Eight-week old WT, stargazin $KI^{+/NL}$ and $KI^{VL/VL}$ mice were anesthetized with isoflurane
824 and euthanized by decapitation. Tissue lysates and post-synaptic density (PSD)
825 isolations were carried out as described below. All procedures were performed at 4 °C.

826 ***Hippocampal lysates***

827 Hippocampi from WT, $KI^{+/NL}$ and $KI^{VL/VL}$ mice were mechanically homogenized in TEEN
828 buffer (25 mM Tris pH 7.4, 1mM EDTA, 1 mM EGTA, 150 mM NaCl and 1% Triton X-
829 100, supplemented with 1 mM DTT, 0.2 mM PMSF, 1 µg/ml CLAP (1 mg/ml of
830 Chymostatin, Leupeptin, Antipain and Pepstatin), 5 mM NaF and 0.1mM Na_3VO_4), using
831 a motor driven glass-Teflon homogenizer at 900 rpm (50 strokes). Hippocampal
832 homogenates were centrifuged at 700 g for 10 minutes and the supernatants were
833 collected and sonicated using an ultrasonic probe for 60 seconds (6 pulses of 5
834 seconds). The samples were again centrifuged at 21100 g for 10 minutes and the
835 supernatants were collected.

836 ***Whole brain lysates and PSD isolations***

837 Cortices and whole brain samples from WT, $KI^{+/NL}$ and $KI^{VL/VL}$ were dissected and
838 homogenized in HEPES A buffer (4 mM HEPES pH=7.4, 0.32 M sucrose, supplemented
839 with 1 mM DTT, 0.2 mM PMSF, 1 µg/ml CLAP, 5 mM NaF and 0.1mM Na_3VO_4), using
840 a motor driven glass-Teflon homogenizer at 900 rpm (50 strokes). These homogenates
841 were centrifuged at 700 x g for 15 minutes. The whole brain lysates and a fraction of the
842 cortical lysates were collected in 2% SDS and 2.5 M Urea and stored at -80 °C for later
843 analysis. The remaining cortical lysate was subjected to the PSD isolation protocol
844 previously described in ⁶⁵. Briefly, the lysates were centrifuged at 18000 x g for 15 min,
845 resulting in the crude synaptosomal pellet, which was re-homogenized in HEPES A

846 buffer and further centrifuged at 25000 x g for 20 min. This yielded the lysed
847 synaptosomal membrane pellet. A fraction of this synaptosomal membrane lysate (SML)
848 was collected in HEPES B buffer (50 mM HEPES pH7.4, 2 mM EDTA, 0.5% Triton X-
849 100, supplemented with 1 mM DTT, 0.2 mM PMSF, 1 µg/ml CLAP, 5 mM NaF and
850 0.1mM Na₃VO₄) and 2% SDS and stored at -80 °C for later analysis. The remaining
851 synaptosomal membrane fraction was resuspended and incubated in HEPES B buffer
852 for 15 min and centrifuged at 32000 x g for 20 min. The resulting pellet was resuspended
853 and incubated in HEPES B buffer for 15min and centrifuged at 200000 x g for 20 min.
854 The resulting pellet, consisting of the PSD fraction, was collected in HEPES B buffer and
855 2% SDS, 2.5 M urea and stored at -80 °C for later analysis.

856 ***Cortical lysates for immunoprecipitation***

857 Cortical lysates for immunoprecipitation were obtained as previously described ⁶⁶.
858 Briefly, fresh cortices from WT or KI^{VL/VL} littermates were mechanically homogenized in
859 5 ml of buffer A (20 mM HEPES, 0.15 mM EDTA, 0.4 mM EGTA, 10 mM KCl, pH 7.5,
860 supplemented with 1 mM DTT, 0.2 mM PMSF, 1 µg/ml CLAP, 5 mM NaF, 0.1 mM
861 Na₃VO₄) followed by sonication and then centrifuged for 10 min at 860 × g. The resulting
862 supernatant was centrifuged for 30 min at 17000 × g. Buffer A was supplemented with
863 15% sucrose and 5 ml was used to homogenize each pellet with 20 strokes, which was
864 further centrifuged for 10 min at 860 × g to remove genomic DNA. The brain membranes
865 present in the supernatant were centrifuged again for 30 min at 17000 × g. The pellets
866 were solubilized in buffer B (20 mM HEPES, 1% Triton-X100, 150 mM NaCl, 0.15 mM
867 EDTA, 4 mM EGTA, pH 7.5, with the same cocktail of protease and phosphatase
868 inhibitors) with 20 dunces with a potter and centrifuged at 17000 x g for 45 minutes,
869 yielding the cortical lysates.

870 **Stargazin immunoprecipitation**

871 Immunoprecipitation (IP) of stargazin was performed as previously described ⁶⁶. Briefly,
872 protein concentration of cortical lysates was quantified with a Bicinchoninic Acid (BCA)

873 assay (Fisher Scientific, USA). The lysates (500 µg) were incubated with the anti-
874 stargazin antibody (IP+) (AB-9876, Merck Millipore, 2 µg) or with normal Rabbit
875 polyclonal IgG (IP-) (12-370, Merck Millipore, 2 µg) for 1 h at 4 °C under rotation and then
876 incubated overnight with 50 µl of protein-A Sepharose at 4 °C. Resin was washed with
877 1 ml of buffer B and 0,5 ml of the same buffer supplemented with 500 mM NaCl. Beads
878 were resuspended in 50 µl of 2x denaturing buffer (62.5 mM Tris·HCl (pH 6.8), 10%
879 Glycerol, 2% SDS, 0.01% bromophenol blue, and 5% β-mercaptoethanol).

880 **Lambda phosphatase treatment**

881 Lambda phosphatase (λ-PP) treatment of cortical PSD samples was performed using
882 the λ-PP treatment kit from New England Biolabs (USA), according to the manufacturer's
883 instructions. In brief, cortical lysates from WT, stargazin KI^{+VL} and KI^{VL/VL} mice were
884 obtained according to the previously described protocol, without the supplementation
885 with the phosphatase inhibitors NaF and Na₃VO₄. The lysates were then divided into two
886 groups: treated and untreated samples. The cortical lysates from the untreated group
887 were supplemented with 5 mM NaF and 0.1mM Na₃VO₄. Samples from the treated group
888 were supplemented with 12.5% of NEBuffer for Protein MetalloPhosphatases (PMP),
889 12.5% of 10mM MnCl₂ and 2.5% of Lambda Protein Phosphatase. All samples from both
890 groups were then incubated at 30 °C for 30 min and processed according to the
891 previously described PSD isolation protocol.

892 **SDS-PAGE and Western blot**

893 Protein quantification was performed using the BCA assay (Fisher Scientific, USA).
894 Samples were denatured with sample buffer 5x (NZYTech, Portugal) and resolved by
895 SDS-PAGE in Tris-glycine-SDS buffer (25 mM Tris, 192 mM glycine, 0.1 % SDS, pH 8.3)
896 in an 11% polyacrylamide gel. Stargazin immunoprecipitation samples were resolved in
897 4-20% Mini-PROTEAN® TGX™ Precast Protein Gels (BioRad) in the same Tris-glycine-
898 SDS buffer. All SDS-PAGE gels were subjected to an overnight electrotransfer (40 V, 4

899 °C) to a PVDF membrane (Millipore, USA). The membranes were then blocked using a
 900 5% milk solution in TBS (20 mM Tris, 137 mM NaCl, pH 7.6) supplemented with 0.1%
 901 Tween-20 (TBS-T) for 1h at room temperature (RT). After blocking, the membranes were
 902 incubated with the primary antibodies against stargazin (AB-9876, Merck Millipore, 1:750
 903 in 3% Milk TBS-T), GluA1 (MAB2263, Merck Millipore, 1:1000 in 5% Milk TBS-T), GluA2
 904 (MAB397, Merck Millipore, 1:1000 in 5% Milk TBS-T) and PSD95 (MA1-045,
 905 ThermoFisher Scientific, 1:1000) for 2h at RT. The membranes were washed 3 times for
 906 10 min in TBS-T and then incubated with the appropriate alkaline phosphatase-
 907 conjugated secondary antibody (#115-055-146 or #211-055-109, Jackson
 908 ImmunoResearch, 1:10000 in 5% milk TBS-T) for 45 min at RT. Following 3 washes in
 909 TBS-T, membranes were developed with the alkaline phosphatase substrate ECF (GE
 910 Healthcare, USA) and the fluorescent signal was acquired using a ChemiDoc Gel
 911 Imaging System (Bio-Rad, USA). The results were analyzed using ImageJ (NIH,
 912 Bethesda, Maryland).

913 **Statistical analysis**

914 The normality of population distributions was calculated for each experiment by
 915 comparison with a theoretical normal distribution using the Shapiro-Wilk normality test.
 916 According to this evaluation parametric or non-parametric tests were used, as described
 917 in the figure legends. For all tests, $p < 0.05$ was considered statistically significant.
 918 Analyses were performed using GraphPad (Prism).

919

920 **ACKNOWLEDGEMENTS**

921 This work was supported by a NARSAD Independent Investigator Grant (#23151) and a
922 NARSAD Young Investigator Grant (#20733) from the Brain and Behavior Research
923 Foundation, by a research grant from the Jérôme Lejeune Foundation (#1530), by a
924 Marie Curie Integration Grant (618525), by a Bial Foundation Grant (266/2016), by
925 national funds through the Portuguese Science and Technology Foundation (FCT:
926 UID/NEU/04539/2013, UIDB/04539/2020, POCI-01-0145-FEDER-28541, POCI-01-
927 0145-FEDER-016682, PTDC/QUI-OUT/32243/2017 and CPCA/A0/7302/2020), and by
928 the European Regional Development Fund (ERDF), through the Centro 2020 Regional
929 Operational Programme, under project CENTRO-01-0145-FEDER-000008:BrainHealth
930 2020. GLC, NB, MVR, ME and CAVB were supported by FCT through Ph.D.
931 scholarships SFRH/BD/51962/2012, SFRH/BD/144881/2019, SFRH/BD/129236/2017,
932 SFRH/BD/51958/2012 and SFRH/BD/145457/2019, respectively. ASI and JG were
933 supported by FCT through Post-doctoral fellowship SFRH/BPD122299/2016 and
934 SFRH/BPD/120611/2016, respectively. RPG and RM received support from FCT/DGES,
935 under the program “Verão com Ciência”. We thank Luisa Cortes and the MICC team for
936 assistance with microscopy imaging; Jorge Valero and Jeannette Schmidt for designing
937 and optimizing quantification macros in Fiji ®; Lara Franco, Nuno Fonseca and Orsolya
938 Antal for technical help. R1 ES cells for mice generation were a kind gift from Dr. Andras
939 Nagy (Mount Sinai Hospital); Stargazin plasmids were a kind gift from Dr. Daniel Choquet
940 (IINS, Bordeaux). Schematic figures were created using Biorender.com. We thank all
941 Ana Luísa Carvalho’s lab members for technical assistance and for the indispensable
942 discussion of the work.

943

944 **AUTHOR CONTRIBUTIONS**

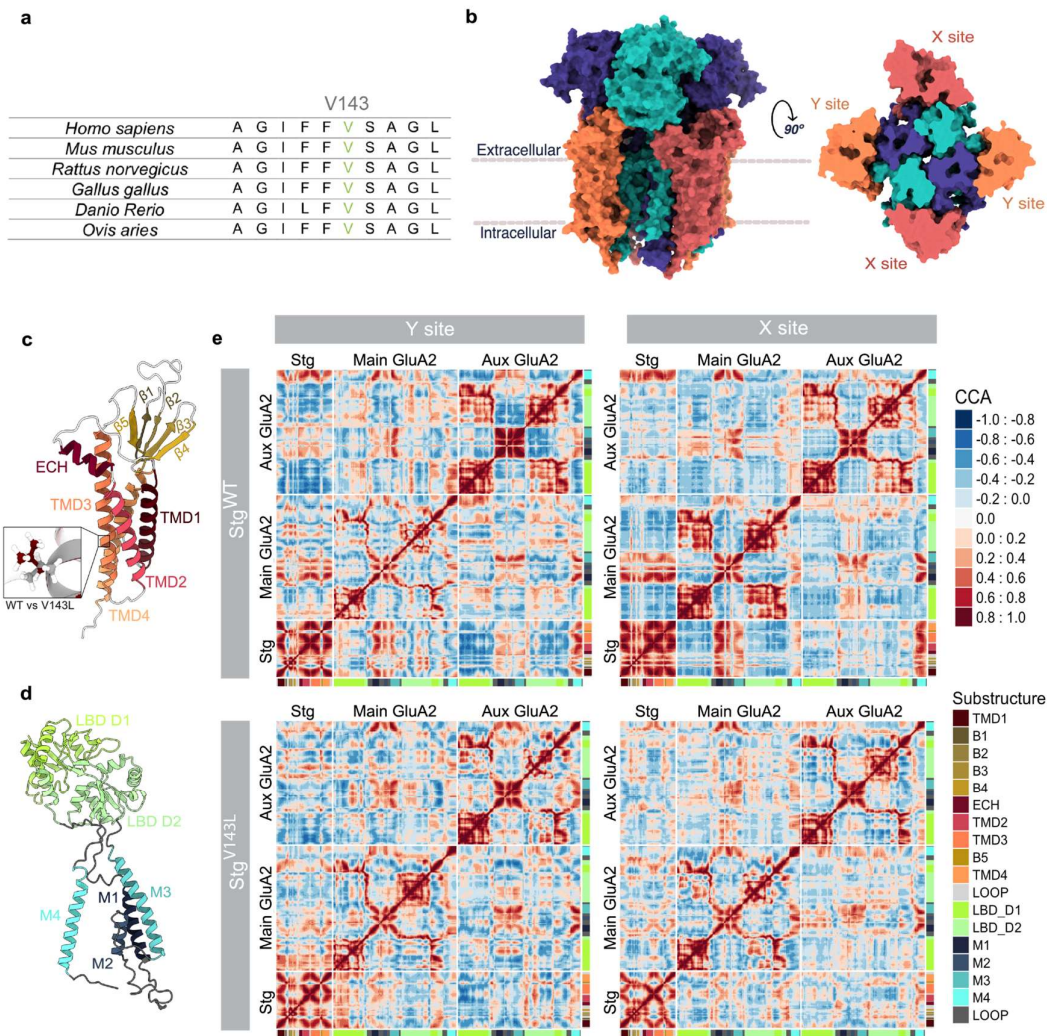
945 Conceptualization, ALC, JP, ISM, GLC, ASI; Methodology, ALC, JP, GLC; Investigation,
 946 GLC, ASI, NB, CAVB, MVR, TR, RM, RPG, BC, SRL; Writing – Original Draft, ALC, GLC,
 947 ASI, NB, ISM; Funding Acquisition, ALC, JP, ISM; Supervision, ALC, JP, ISM.
 948

949 **DECLARATION OF INTERESTS**

950 The authors declare no competing interests.

951 **FIGURES**

952



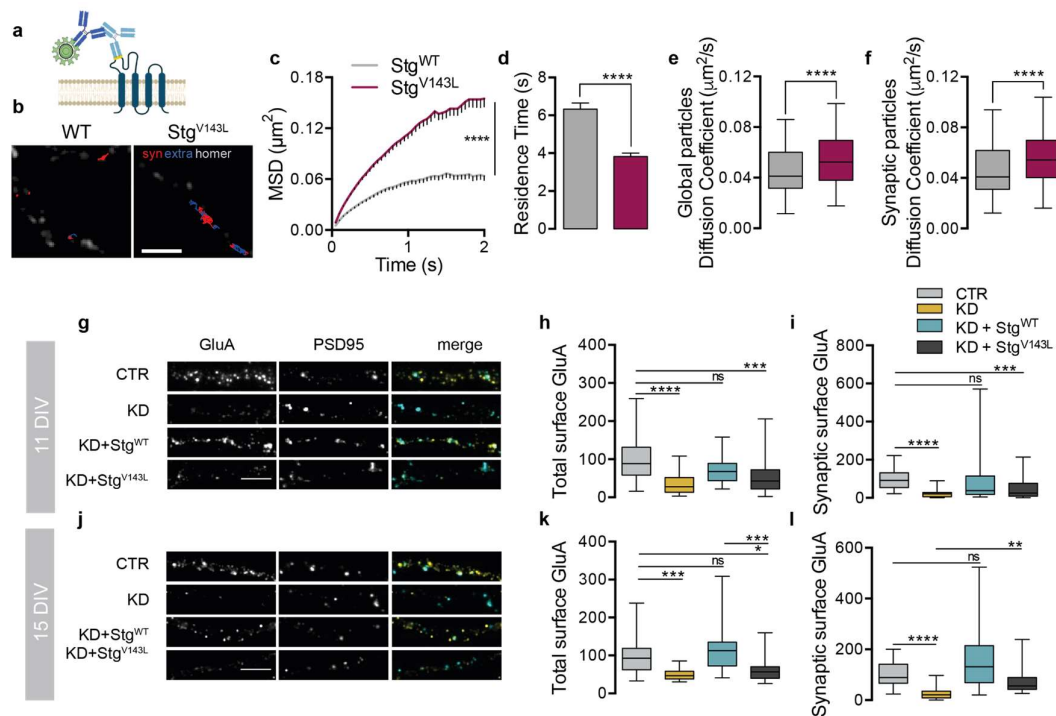
953

954 **Figure 1. The ID-associated stargazin mutation in the highly conserved V143**
955 **residue weakens the interaction between stargazin and AMPARs.**

956 **(a)** Valine 143 in stargazin is highly conserved among species. **(b)** Surface
957 representation of AMPAR:stargazin complex viewed parallel to the membrane (left) and
958 from the extracellular side (right). The extracellular view of the complex (at the membrane
959 level) shows the two different sets of stargazin assembly points (X and Y sites) around

960 AMPAR. Each GluA subunit is colored individually in shades of blue. Stargazin
 961 molecules are colored in orange (Y site) or brick (X site). **(c)** Side view of the stargazin
 962 structure shown as a cartoon with substructures labelled and colored in a spectrum of
 963 yellow/orange. Close-up shows the V143L mutation (WT – grey; ID – red). **(d)** Side view
 964 of a GluA2 subunit structure shown as cartoon with substructures labelled and
 965 transmembrane domains colored in a spectrum of blue and ligand-binding domain
 966 colored in green. **(e)** Dynamical cross-correlation maps for the AMPAR:stargazin
 967 complex WT form in Y site and X site and for stargazin V143L form in the Y and X sites.
 968 Substructure annotation was added at the bottom and right of each map for easier
 969 reading. CCA goes from -1 (anticorrelated, opposite direction) to 1 (correlated, same
 970 direction). See also Figs. S1-S4.

971



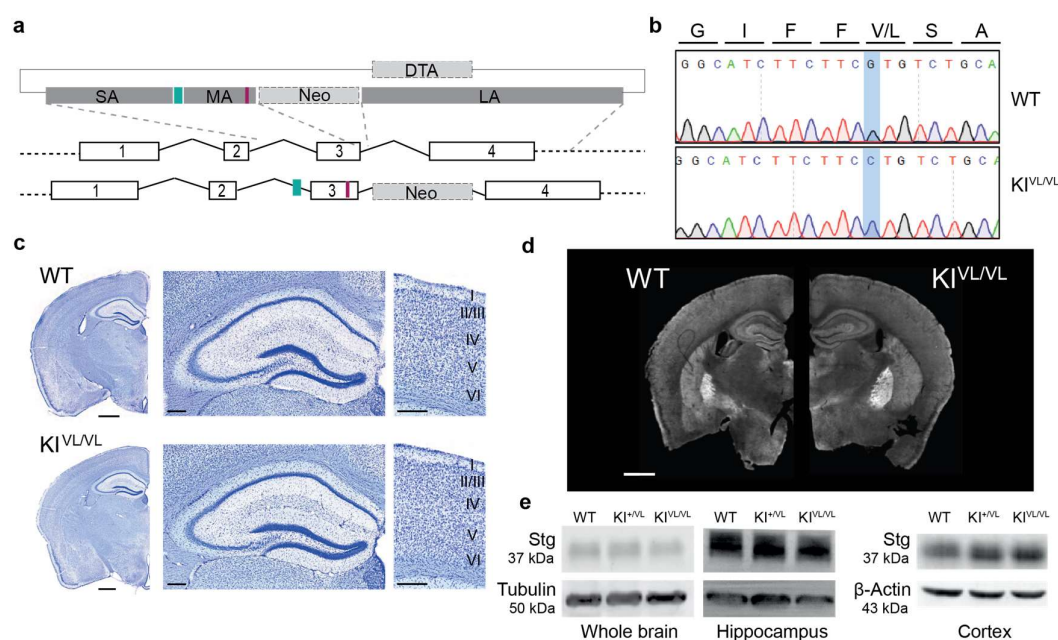
972

973

974 **Figure 2. Stargazin ID-associated variant presents altered surface diffusion and**
 975 **elicits defective AMPAR trafficking.**

976 **(a)** Cortical neurons were co-transfected with Homer1C-GFP and HA-stargazin
 977 (either the WT form of stargazin – Stg^{WT} – or the intellectual disability-associated variant
 978 – Stg^{V143L}). Stargazin surface diffusion was evaluated using quantum dot (QD)-labelled
 979 secondary antibodies (dark blue) against anti-HA antibodies (light blue) to detect the
 980 extracellular HA epitope (yellow) in stargazin (HA-stargazin). **(b)** Reconstructed HA-
 981 stargazin trajectories (synaptic and perisynaptic - red, extrasynaptic - blue) and
 982 Homer1C-GFP signal (white). Scale bar represents 5 μm . **(c)** Stargazin mean square
 983 displacement (MSD) (\pm SEM) versus time plots for cells expressing WT stargazin or the
 984 V143L variant. **** p < 0.0001 by Mann Whitney test. **(d)** Mean synaptic residence time
 985 (\pm SEM) of WT stargazin and stargazin V143L. **** p < 0.0001 by unpaired t-test. **(e, f)**
 986 Surface diffusion coefficient of global (e) and synaptic (f; Homer1C-GFP-colocalized)
 987 single QD-stargazin particles. Median diffusion (\pm 25%–75% IQR) of 277 and 485 for

988 global trajectories, respectively and 139 and 280 for synaptic trajectories, respectively.
989 **** $p < 0.0001$ by unpaired t-test. A minimum of 18 cells were analyzed from 3
990 independent experiments. **(g-l)** Disrupted AMPAR surface expression in the presence of
991 the stargazin V143L variant. Low-density cortical neurons were transfected at 7 **(g,h,i)**
992 or 11 **(j,k,l)** days *in vitro* (DIV) with a control plasmid (pLL-shRNA-CTR) or with pLL-
993 shRNA-Stg, which downregulates endogenous stargazin expression, or co-transfected
994 with pLL-shRNA-Stg and pcDNA-Stg^{WT} or pcDNA-Stg^{V143L}. Total surface and synaptic
995 levels of GluA subunits were analyzed by immunocytochemistry at DIV11 or DIV15. **(g,j)**
996 Representative images of GluA distribution and quantification of total **(h,k)** and synaptic
997 **(i,l)** intensity of GluA clusters show impaired trafficking of AMPAR in neurons where
998 stargazin was silenced, or which expressed the Stg^{V143L} variant. GluA accumulation at
999 synaptic sites was assessed by the colocalization with PSD95 clusters. Clusters from 11
1000 DIV cells were quantified from at least 33 cells imaged from four independent
1001 experiments; clusters from 15 DIV cells were quantified from 20 cells from two
1002 independent experiments. **** $p < 0.0001$; *** $p < 0.001$; two-way ANOVA, followed by
1003 Dunn's multiple comparison post hoc test. Boxes show the 25th and 75th percentiles,
1004 whiskers range from the minimum to the maximum values, and the horizontal line in each
1005 box shows the median value. Scale bars represent 5 μ m.
1006



1007

1008

1009 **Figure 3. Stargazin V143L knock-in mice express normal stargazin levels and**
 1010 **present no gross brain abnormalities.**

1011 **(a)** Strategy for generating stargazin V143L knock-in mice. A vector containing two
 1012 selection markers, Neo and DTA, and three homology arms was constructed: the short
 1013 (SA) and the long arm (LA) allowed homologous recombination with the genomic DNA
 1014 of mouse embryonic stem (ES) cells, and the middle arm (MA) contained the ID-
 1015 associated point mutation (V143L) (red bar). A forward primer designed against a
 1016 synthetic random sequence (non-existing in the mouse genome – green bar), inserted
 1017 upstream the middle arm, allows genotyping of the animals. **(b)** The directed
 1018 mutagenesis was confirmed by Sanger sequencing of the third exon in WT and
 1019 homozygous stargazin KI^{VL/VL} animals. **(c)** Cresyl violet staining of brain slices from WT
 1020 and stargazin KI^{VL/VL} animals showed no gross differences. Scale bar represents 1000
 1021 μ m for lower magnification images and 200 μ m for magnified images. **(d)** The brain
 1022 expression pattern of stargazin in WT and stargazin KI^{VL/VL} animals was assessed by
 1023 immunohistochemistry. Scale bar represents 1000 μ m. **(e)** Total stargazin levels in the

1024 whole brain, hippocampal and cortical lysates from WT and stargazin V143L KI animals
1025 were evaluated by Western blot. See also Fig. S5.
1026

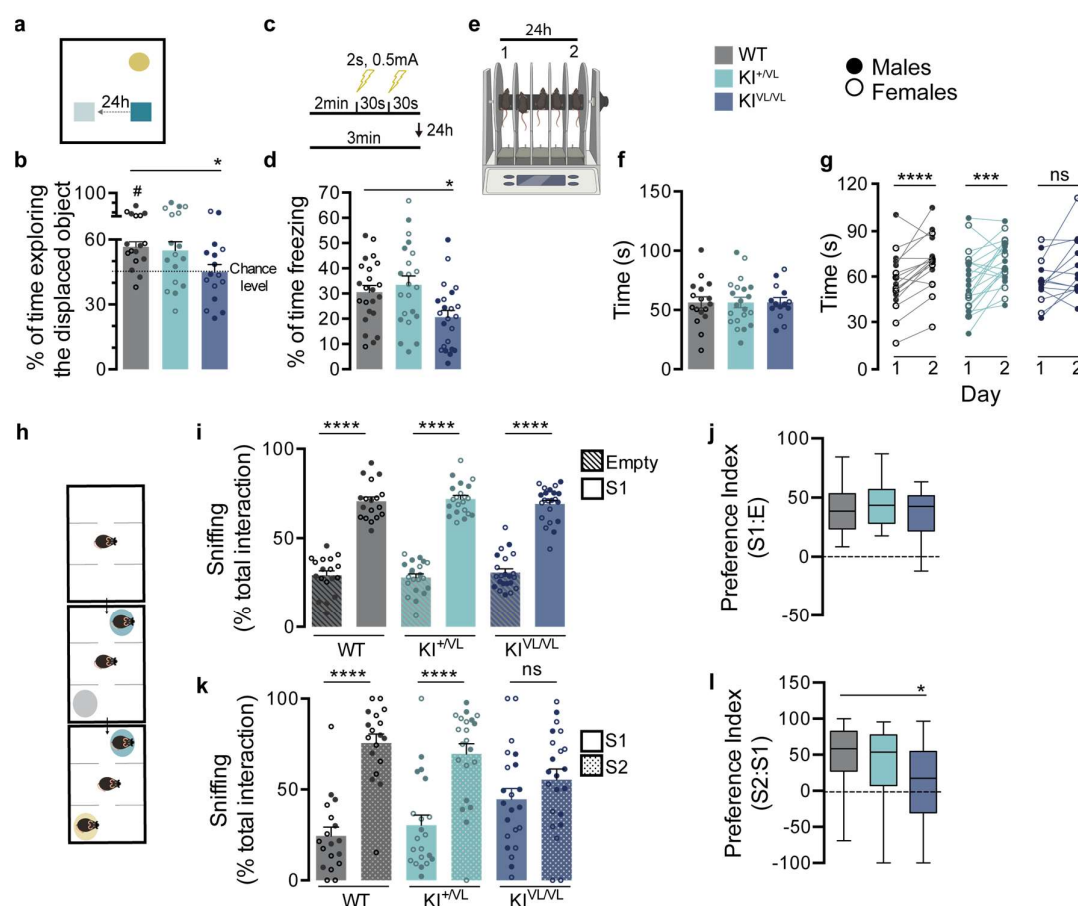
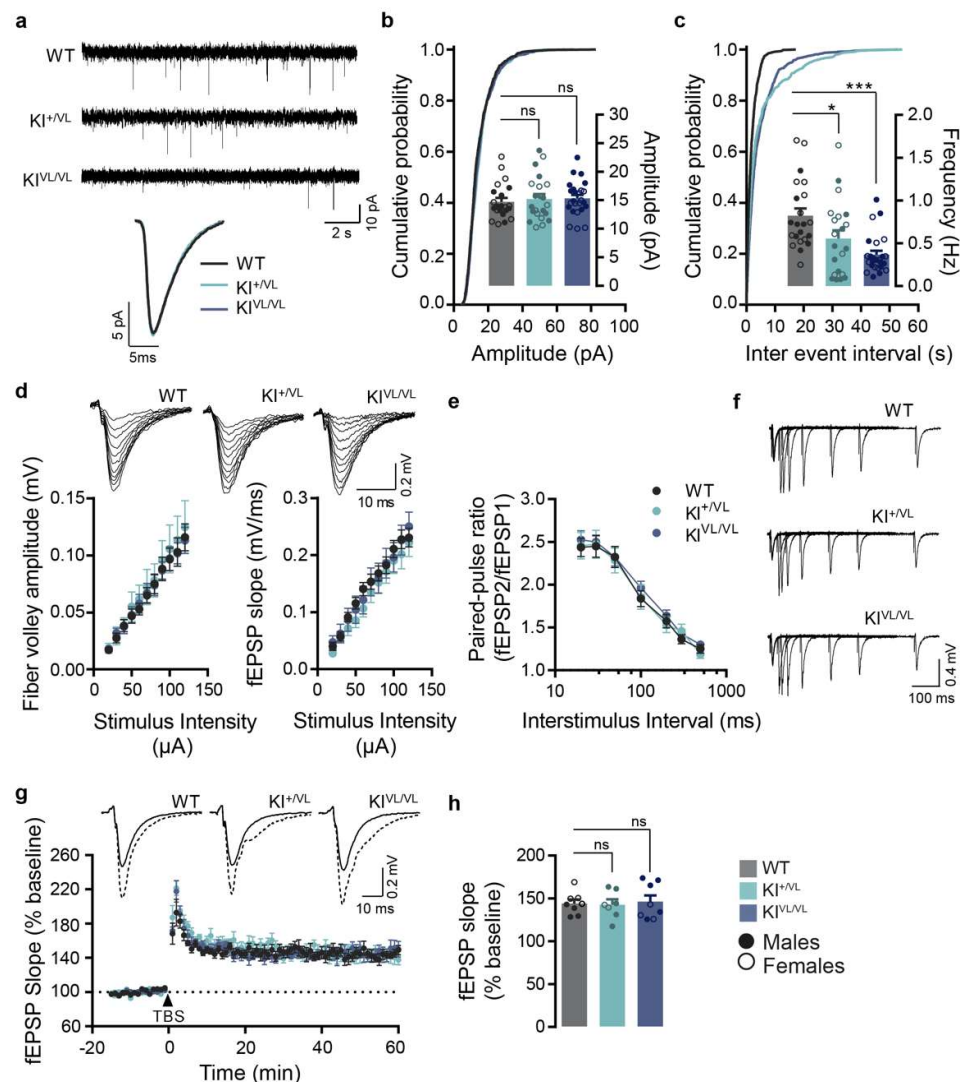


Figure 4. Stargazin V143L KI mice show cognitive and social deficits.

(a, b) When subjected to the object displacement recognition test, homozygous stargazin V143L (KI^{VL/VL}) mice spent less time exploring the displaced object when compared to their WT counterparts, and did not have preference for the displaced object. Data are presented as mean ± SEM. *p < 0.05, One-way ANOVA followed by Dunnett's multiple comparison post hoc test, #p < 0.05, One-sample t-test to the value of 50%. n ≥ 16 (males and females) for all genotypes. (c, d) Homozygous stargazin V143L knock-in mice presented significantly less freezing behavior than WT counterparts in the contextual fear conditioning test. Data are presented as mean ± SEM. *p ≤ 0.05, One-way ANOVA followed by Dunnett's multiple comparison post-hoc test. n ≥ 22 (males and females) for all genotypes. (e) Motor function and learning were evaluated using the rotarod test. (f)

1040 The average time spent on the rotarod did not significantly vary between genotypes. **(g)**
1041 Both WT and heterozygous stargazin V143L (KI^{+VL}) animals performed significantly
1042 better in the second day, whereas stargazin $KI^{VL/VL}$ mice failed to show motor learning.
1043 *** $p < 0.001$, **** $p < 0.0001$, Ratio paired t-test, $n \geq 14$ for all genotypes (males and
1044 females). **(h)** Mice were submitted to the three-chamber social interaction paradigm. The
1045 time spent approaching the cages, with and without the stranger stimulus mouse, was
1046 evaluated for 10 and 5 minutes, respectively. **(i,j)** All animals displayed social preference,
1047 but **(k,l)** stargazin $KI^{VL/VL}$ mice showed no preference for a new stranger mouse in the
1048 arena, unlike WT and heterozygous stargazin V143L mice. Data are presented as mean
1049 \pm SEM **(i, k)** and median with range **(j, l)**. **(i, k)** **** $p < 0.0001$, Two-way ANOVA followed
1050 by Sidak's multiple comparison post-hoc test. $n \geq 13$ (males and females) for all
1051 genotypes. **(j, l)** * $p \leq 0.05$, Kruskal-Wallis followed by Dunn's multiple comparison post-
1052 hoc test. $n \geq 13$ (males and females) for all genotypes. See also Fig. S6.
1053



1054

1055 **Figure 5. Decreased frequency of AMPAR-mediated mEPSCs in CA1 pyramidal**
 1056 **neurons in stargazin V143L KI mice.**

1057 **(a)** Representative traces of mEPSCs recordings and single average event of CA1
 1058 pyramidal neurons in acute hippocampal slices from WT, stargazin KI^{+/VL} and stargazin
 1059 KI^{VL/VL} mice. Cumulative probability distribution and average mEPSCs amplitude **(b)** and
 1060 frequency **(c)** plots, showing a reduction in frequency but not amplitude of mEPSCs in
 1061 stargazin V143L KI mice (P15-P20). Data are presented as mean \pm SEM. * p < 0.05, *** p
 1062 < 0.001, ns, not significant, Kruskal-Wallis followed by Dunn's multiple comparison post-

1063 hoc test. n = 22 cells/10 animals (4 males and 6 females) for WT mice, n = 21 cells/8
1064 animals (4 males and 4 females) for KI^{+/-} mice, n = 25 cells/6 animals (3 males and 3
1065 females) for KI^{VL/VL} mice. **(d)** Representative traces of evoked fEPSPs at CA1 synapses
1066 on hippocampal slices from P15-P20 WT and stargazin V143L KI mice, upon stimulation
1067 of CA3 pyramidal neurons Schaffer collaterals. Plots show the mean \pm SEM of fiber
1068 volley amplitude and fEPSP slopes. Input-output curves were similar for all genotypes,
1069 indicating that evoked basal transmission in this synapse is not impaired in stargazin
1070 V143L KI mice. n = 17 slices/10 animals (5 male and 5 female) for WT mice, n = 11
1071 slices/8 animals (4 male and 4 female) for stargazin KI^{+/-} mice, n = 15 slices/10 animals
1072 (6 male and 4 female) for stargazin KI^{VL/VL} mice. **(e)** Paired-pulse facilitation at SC-CA1
1073 synapses in stargazin V143L KI mice was not altered. Data are presented as mean \pm
1074 SEM. n = 8 slices/6 animals (3 males and 3 females) for WT mice, n = 7 slices/5 animals
1075 (3 males and 2 females) for stargazin KI^{+/-} mice, n = 8 slices/5 animals (3 males and 2
1076 females) for stargazin KI^{VL/VL} mice. **(f)** Representative traces of paired-pulse stimulation
1077 evoked fEPSPs in WT and stargazin V143L KI mice. **(g)** LTP induced by theta burst
1078 stimulation (TBS) at SC-CA1 synapses was comparable between genotypes. Insets
1079 show representative traces of evoked fEPSPs before (solid lines) and after (dashed
1080 lines) LTP induction. Data are presented as mean \pm SEM. n = 8 slices/6 animals (3 males
1081 and 3 females) for WT mice, n = 7 slices/5 animals (3 males and 2 females) for stargazin
1082 KI^{+/-} mice, n = 8 slices/5 animals (3 males and 2 females) for stargazin KI^{VL/VL} mice. **(h)**
1083 Average fEPSP slope in the last 10 min of the recording post LTP-induction. Data are
1084 presented as mean \pm SEM. ns, not significant, One-way ANOVA followed by Dunnett's
1085 multiple comparison post-hoc test.

1086

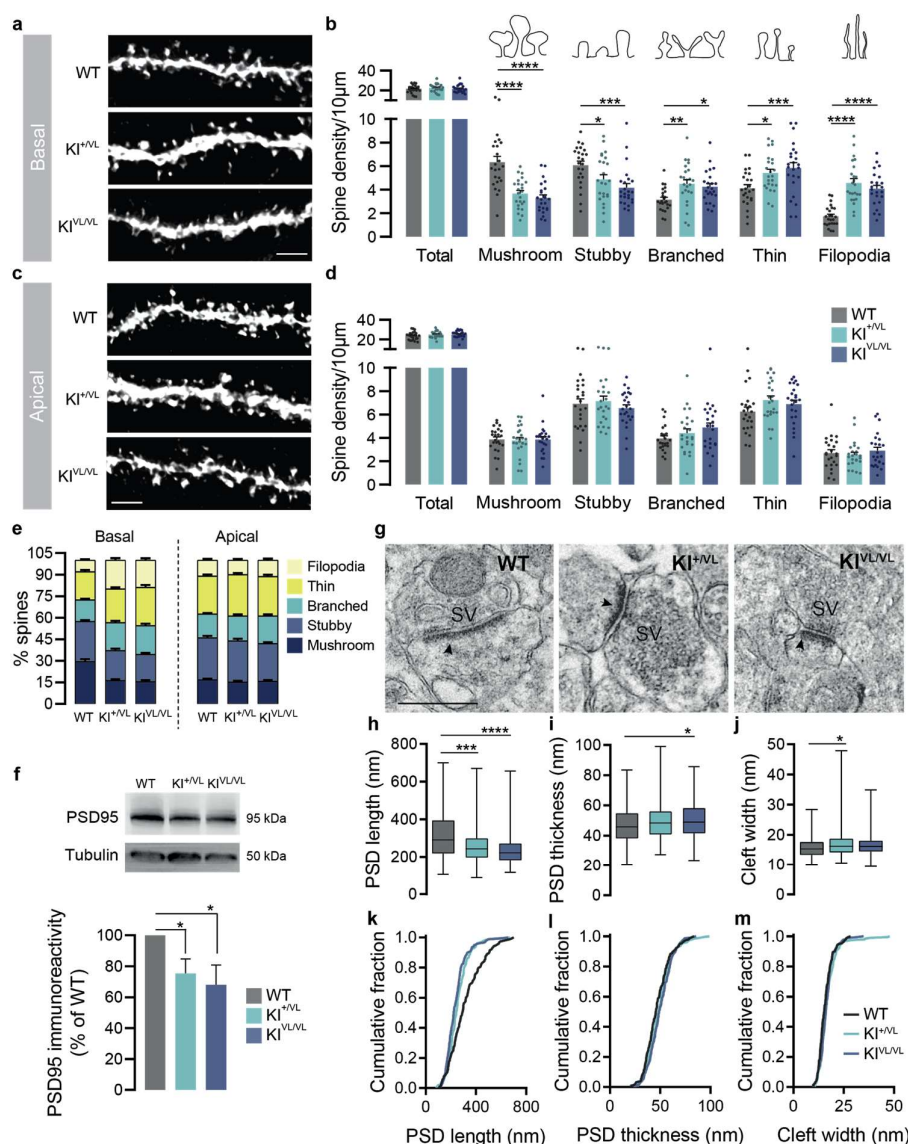


Figure 6. Stargazin V143L KI mice present alterations in hippocampal spine morphology and PSD ultrastructure.

(a-e) Although no changes were observed in the density of spines from both basal and apical dendrites in CA1 neurons, stargazin V143L KI animals presented a decrease in mushroom and stubby spines and an increase in branched, thin and filopodia spines, in basal dendrites, indicating a defect in spine maturation. Data are presented as mean ± SEM (b, d) or as percentage of the total number of spines (e). *p < 0.05, **p < 0.01, ***p

1096 < 0.001, **** p < 0.0001, Two-way repeated measures ANOVA followed by Dunnett's
1097 multiple comparison post-hoc test. n = 24 branches/3 animals for all genotypes. Scale
1098 bar represents 2 μ m. **(f)** Immunostaining of PSD95 by Western blot showed a significant
1099 decrease of its levels in hippocampal samples from stargazin V143L KI mice compared
1100 to WT controls. * p < 0.05, One-sample t-test to the value of 100%. The staining of tubulin
1101 of hippocampi samples is the same presented in Figure 3e. **(g)** Representative electron
1102 transmission microscopy images of hippocampal synapses from WT, stargazin KI^{+/-} and
1103 stargazin KI^{VL/VL} animals, and **(h,k)** quantification of post-synaptic density length, **(i,l)**
1104 thickness and **(j,m)** cleft width. Data are presented as median with range. * p < 0.05, *** p
1105 < 0.001, **** p < 0.0001, Kruskal-Wallis followed by Dunn's multiple comparison post hoc-
1106 test. n = 153 PSDs/2 animals for WT mice, n = 203 PSDs/2 animals for KI^{+/-} mice, n =
1107 236 cells/2 animals for KI^{VL/VL} mice. The arrows indicate post-synaptic densities. SV,
1108 synaptic vesicles. Scale bar represents 500 nm. See also Figs. S7 and S8.
1109

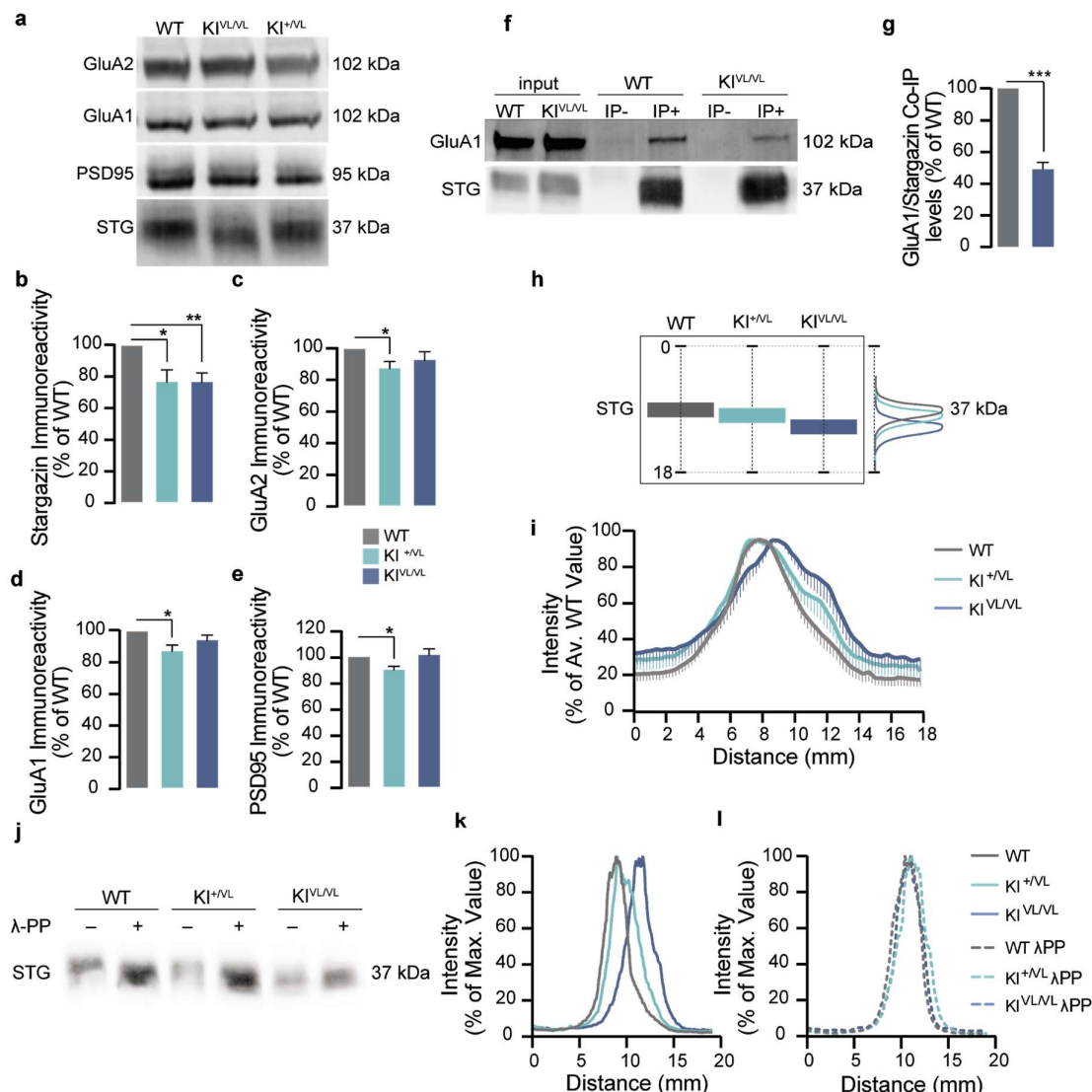


Figure 7. Stargazin V143L expression modifies the composition of PSDs.

(a) Western blot analysis of cortical PSDs (see also Fig. S8j) showed that heterozygous stargazin KI^{+/VL} animals and homozygous stargazin KI^{VL/VL} mice have decreased synaptic levels of stargazin (b). GluA2 (c), GluA1 (d) and PSD95 (e) levels were also reduced in the PSDs of stargazin KI^{+/VL} animals. Data were normalized for WT values and are presented as mean ± SEM. One-sample t-test to the value of 100%. * $p \leq 0.05$, ** $p < 0.01$, $n \geq 6$ for all conditions. (f) Immunoprecipitation of stargazin from the cortices of WT and stargazin KI^{VL/VL} animals. (g) Co-immunoprecipitation of GluA1 with stargazin

1120 significantly reduced in the KI^{VL/VL} cortices. Data were normalized for immunoprecipitated
1121 stargazin in each respective condition. Data normalized to WT values and presented as
1122 mean \pm SEM. One-sample t-test to the value of 100%, *** p < 0.001, n = 5 for all
1123 conditions. **(h)** The SDS-PAGE migration pattern of stargazin from WT, stargazin KI^{+^{VL}}
1124 and KI^{VL/VL} mouse cortical PSD extracts **(a)** was analyzed by quantifying the distribution
1125 of the intensity of the bands along the length of the lane. **(i)** In PSDs isolated from
1126 stargazin KI^{VL/VL} animals, stargazin migrated faster in the SDS-PAGE. Data were
1127 normalized for the average maximum intensity of WT stargazin for each western blot
1128 membrane and are presented as mean \pm SEM, n = 9. **(j)** Representative images from
1129 stargazin labelling profile in cortical PSD samples isolated from WT, stargazin KI^{+^{VL}} and
1130 KI^{VL/VL} samples non-treated **(k)** or treated **(l)** with λ -Phosphatase. λ -Phosphatase
1131 treatment of isolated cortical PSDs induced a shift in the apparent molecular weight of
1132 stargazin in WT and stargazin KI^{+^{VL}} PSD samples, but not in stargazin KI^{VL/VL} PSD
1133 samples, suggesting deficient phosphorylation of the stargazin V143L protein variant
1134 detectable in homozygous stargazin V143L KI animals.
1135

1136 REFERENCES

- 1137 1 Greger, I. H., Watson, J. F. & Cull-Candy, S. G. Structural and Functional
1138 Architecture of AMPA-Type Glutamate Receptors and Their Auxiliary Proteins.
1139 *Neuron* **94**, 713-730, doi:10.1016/j.neuron.2017.04.009 (2017).
- 1140 2 Jackson, A. C. & Nicoll, R. A. The expanding social network of ionotropic
1141 glutamate receptors: TARPs and other transmembrane auxiliary subunits.
1142 *Neuron* **70**, 178-199, doi:10.1016/j.neuron.2011.04.007 (2011).
- 1143 3 Jacobi, E. & von Engelhardt, J. Diversity in AMPA receptor complexes in the
1144 brain. *Curr Opin Neurobiol* **45**, 32-38, doi:10.1016/j.conb.2017.03.001 (2017).
- 1145 4 Tomita, S. *et al.* Functional studies and distribution define a family of
1146 transmembrane AMPA receptor regulatory proteins. *J Cell Biol* **161**, 805-816,
1147 doi:10.1083/jcb.200212116 (2003).
- 1148 5 Letts, V. A. *et al.* The mouse stargazer gene encodes a neuronal Ca²⁺-channel
1149 gamma subunit. *Nature genetics* **19**, 340-347, doi:10.1038/1228 (1998).
- 1150 6 Hashimoto, K. *et al.* Impairment of AMPA receptor function in cerebellar granule
1151 cells of ataxic mutant mouse stargazer. *J Neurosci* **19**, 6027-6036 (1999).
- 1152 7 Chen, L. *et al.* Stargazin regulates synaptic targeting of AMPA receptors by two
1153 distinct mechanisms. *Nature* **408**, 936-943, doi:10.1038/35050030 (2000).
- 1154 8 Bats, C., Groc, L. & Choquet, D. The interaction between Stargazin and PSD-95
1155 regulates AMPA receptor surface trafficking. *Neuron* **53**, 719-734,
1156 doi:10.1016/j.neuron.2007.01.030 (2007).
- 1157 9 Zeng, M. *et al.* Phase Separation-Mediated TARP/MAGUK Complex
1158 Condensation and AMPA Receptor Synaptic Transmission. *Neuron* **104**, 529-543
1159 e526, doi:10.1016/j.neuron.2019.08.001 (2019).
- 1160 10 Louros, S. R., Caldeira, G. L. & Carvalho, A. L. Stargazin Dephosphorylation
1161 Mediates Homeostatic Synaptic Downscaling of Excitatory Synapses. *Front Mol*
1162 *Neurosci* **11**, 328, doi:10.3389/fnmol.2018.00328 (2018).

1163 11 Louros, S. R., Hooks, B. M., Litvina, L., Carvalho, A. L. & Chen, C. A role for
1164 stargazin in experience-dependent plasticity. *Cell Rep* **7**, 1614-1625,
1165 doi:10.1016/j.celrep.2014.04.054 (2014).

1166 12 Tomita, S., Stein, V., Stocker, T. J., Nicoll, R. A. & Bredt, D. S. Bidirectional
1167 synaptic plasticity regulated by phosphorylation of stargazin-like TARPs. *Neuron*
1168 **45**, 269-277, doi:10.1016/j.neuron.2005.01.009 (2005).

1169 13 Lima Caldeira, G., Peca, J. & Carvalho, A. L. New insights on synaptic
1170 dysfunction in neuropsychiatric disorders. *Curr Opin Neurobiol* **57**, 62-70,
1171 doi:10.1016/j.conb.2019.01.004 (2019).

1172 14 Fromer, M. *et al.* De novo mutations in schizophrenia implicate synaptic
1173 networks. *Nature* **506**, 179-184, doi:10.1038/nature12929 (2014).

1174 15 Hall, J., Trent, S., Thomas, K. L., O'Donovan, M. C. & Owen, M. J. Genetic Risk
1175 for Schizophrenia: Convergence on Synaptic Pathways Involved in Plasticity. *Biol*
1176 *Psychiatry* **77**, 52-58, doi:10.1016/j.biopsych.2014.07.011 (2015).

1177 16 Hamdan, F. F. *et al.* Excess of de novo deleterious mutations in genes associated
1178 with glutamatergic systems in nonsyndromic intellectual disability. *Am J Hum*
1179 *Genet* **88**, 306-316, doi:10.1016/j.ajhg.2011.02.001 (2011).

1180 17 Kirov, G. *et al.* De novo CNV analysis implicates specific abnormalities of
1181 postsynaptic signalling complexes in the pathogenesis of schizophrenia.
1182 *Molecular psychiatry* **17**, 142-153, doi:10.1038/mp.2011.154 (2012).

1183 18 Sanders, S. J. *et al.* Insights into Autism Spectrum Disorder Genomic
1184 Architecture and Biology from 71 Risk Loci. *Neuron* **87**, 1215-1233,
1185 doi:10.1016/j.neuron.2015.09.016 (2015).

1186 19 Liu, Y. L. *et al.* RASD2, MYH9, and CACNG2 genes at chromosome 22q12
1187 associated with the subgroup of schizophrenia with non-deficit in sustained
1188 attention and executive function. *Biol Psychiatry* **64**, 789-796,
1189 doi:10.1016/j.biopsych.2008.04.035 (2008).

1190 20 Beneyto, M. & Meador-Woodruff, J. H. Lamina-specific abnormalities of AMPA
1191 receptor trafficking and signaling molecule transcripts in the prefrontal cortex in
1192 schizophrenia. *Synapse* **60**, 585-598, doi:10.1002/syn.20329 (2006).

1193 21 Silberberg, G. *et al.* Stargazin involvement with bipolar disorder and response to
1194 lithium treatment. *Pharmacogenetics and genomics* **18**, 403-412,
1195 doi:10.1097/FPC.0b013e3282f974ca (2008).

1196 22 Miranda, A. *et al.* Study of 45 candidate genes suggests CACNG2 may be
1197 associated with lithium response in bipolar disorder. *Journal of affective disorders*
1198 **248**, 175-179, doi:10.1016/j.jad.2019.01.010 (2019).

1199 23 Adzhubei, I. A. *et al.* A method and server for predicting damaging missense
1200 mutations. *Nat Methods* **7**, 248-249, doi:10.1038/nmeth0410-248 (2010).

1201 24 Kumar, P., Henikoff, S. & Ng, P. C. Predicting the effects of coding non-
1202 synonymous variants on protein function using the SIFT algorithm. *Nature*
1203 *protocols* **4**, 1073-1081, doi:10.1038/nprot.2009.86 (2009).

1204 25 Choi, Y. & Chan, A. P. PROVEAN web server: a tool to predict the functional
1205 effect of amino acid substitutions and indels. *Bioinformatics* **31**, 2745-2747,
1206 doi:10.1093/bioinformatics/btv195 (2015).

1207 26 Hollingsworth, S. A. & Dror, R. O. Molecular Dynamics Simulation for All. *Neuron*
1208 **99**, 1129-1143, doi:10.1016/j.neuron.2018.08.011 (2018).

1209 27 Lazim, R., Suh, D. & Choi, S. Advances in Molecular Dynamics Simulations and
1210 Enhanced Sampling Methods for the Study of Protein Systems. *International*
1211 *journal of molecular sciences* **21**, doi:10.3390/ijms21176339 (2020).

1212 28 Twomey, E. C., Yelshanskaya, M. V., Vassilevski, A. A. & Sobolevsky, A. I.
1213 Mechanisms of Channel Block in Calcium-Permeable AMPA Receptors. *Neuron*
1214 **99**, 956-968 e954, doi:10.1016/j.neuron.2018.07.027 (2018).

1215 29 Chen, S. & Gouaux, E. Structure and mechanism of AMPA receptor - auxiliary
1216 protein complexes. *Current opinion in structural biology* **54**, 104-111,
1217 doi:10.1016/j.sbi.2019.01.011 (2019).

1218 30 Twomey, E. C., Yelshanskaya, M. V. & Sobolevsky, A. I. Structural and functional
1219 insights into transmembrane AMPA receptor regulatory protein complexes. *The*
1220 *Journal of general physiology* **151**, 1347-1356, doi:10.1085/jgp.201812264
1221 (2019).

1222 31 Vandenberghe, W., Nicoll, R. A. & Bredt, D. S. Interaction with the unfolded
1223 protein response reveals a role for stargazin in biosynthetic AMPA receptor
1224 transport. *J Neurosci* **25**, 1095-1102, doi:10.1523/JNEUROSCI.3568-04.2005
1225 (2005).

1226 32 Schnell, E. *et al.* Direct interactions between PSD-95 and stargazin control
1227 synaptic AMPA receptor number. *Proc Natl Acad Sci U S A* **99**, 13902-13907,
1228 doi:10.1073/pnas.172511199 (2002).

1229 33 Opazo, P. *et al.* CaMKII triggers the diffusional trapping of surface AMPARs
1230 through phosphorylation of stargazin. *Neuron* **67**, 239-252,
1231 doi:10.1016/j.neuron.2010.06.007 (2010).

1232 34 Twomey, E. C., Yelshanskaya, M. V., Grassucci, R. A., Frank, J. & Sobolevsky,
1233 A. I. Elucidation of AMPA receptor-stargazin complexes by cryo-electron
1234 microscopy. *Science* **353**, 83-86, doi:10.1126/science.aaf8411 (2016).

1235 35 Zhao, Y., Chen, S., Yoshioka, C., Bacongus, I. & Gouaux, E. Architecture of fully
1236 occupied GluA2 AMPA receptor-TARP complex elucidated by cryo-EM. *Nature*
1237 **536**, 108-111, doi:10.1038/nature18961 (2016).

1238 36 Forrest, M. P., Parnell, E. & Penzes, P. Dendritic structural plasticity and
1239 neuropsychiatric disease. *Nature reviews. Neuroscience* **19**, 215-234,
1240 doi:10.1038/nrn.2018.16 (2018).

1241 37 Favaro, P. D. *et al.* An opposing function of paralogs in balancing developmental
1242 synapse maturation. *PLoS biology* **16**, e2006838,
1243 doi:10.1371/journal.pbio.2006838 (2018).

1244 38 Cane, M., Maco, B., Knott, G. & Holtmaat, A. The relationship between PSD-95
1245 clustering and spine stability in vivo. *J Neurosci* **34**, 2075-2086,
1246 doi:10.1523/JNEUROSCI.3353-13.2014 (2014).

1247 39 Sumioka, A., Yan, D. & Tomita, S. TARP phosphorylation regulates synaptic
1248 AMPA receptors through lipid bilayers. *Neuron* **66**, 755-767,
1249 doi:10.1016/j.neuron.2010.04.035 (2010).

1250 40 Hafner, A. S. *et al.* Lengthening of the Stargazin Cytoplasmic Tail Increases
1251 Synaptic Transmission by Promoting Interaction to Deeper Domains of PSD-95.
1252 *Neuron* **86**, 475-489, doi:10.1016/j.neuron.2015.03.013 (2015).

1253 41 Rouach, N. *et al.* TARP gamma-8 controls hippocampal AMPA receptor number,
1254 distribution and synaptic plasticity. *Nat Neurosci* **8**, 1525-1533,
1255 doi:10.1038/nn1551 (2005).

1256 42 Menuz, K., O'Brien, J. L., Karmizadegan, S., Bredt, D. S. & Nicoll, R. A. TARP
1257 redundancy is critical for maintaining AMPA receptor function. *J Neurosci* **28**,
1258 8740-8746, doi:10.1523/JNEUROSCI.1319-08.2008 (2008).

1259 43 Yamasaki, M. *et al.* TARP gamma-2 and gamma-8 Differentially Control AMPAR
1260 Density Across Schaffer Collateral/Commissural Synapses in the Hippocampal
1261 CA1 Area. *J Neurosci* **36**, 4296-4312, doi:10.1523/JNEUROSCI.4178-15.2016
1262 (2016).

1263 44 Sali, A. & Blundell, T. L. Comparative protein modelling by satisfaction of spatial
1264 restraints. *Journal of molecular biology* **234**, 779-815,
1265 doi:10.1006/jmbi.1993.1626 (1993).

1266 45 UniProt, C. UniProt: a worldwide hub of protein knowledge. *Nucleic acids*
1267 *research* **47**, D506-D515, doi:10.1093/nar/gky1049 (2019).

1268 46 Sippl, M. J. Recognition of errors in three-dimensional structures of proteins.
1269 *Proteins* **17**, 355-362, doi:10.1002/prot.340170404 (1993).

1270 47 Wiederstein, M. & Sippl, M. J. ProSA-web: interactive web service for the
1271 recognition of errors in three-dimensional structures of proteins. *Nucleic acids*
1272 *research* **35**, W407-410, doi:10.1093/nar/gkm290 (2007).

1273 48 Wallner, B. & Elofsson, A. Can correct protein models be identified? *Protein*
1274 *science : a publication of the Protein Society* **12**, 1073-1086,
1275 doi:10.1110/ps.0236803 (2003).

1276 49 Abraham, M. J., Hess, B., van der Spoel, D., Lindahl, E. & The-GROMACS-
1277 development-team. (2018).

1278 50 Huang, J. & MacKerell, A. D., Jr. CHARMM36 all-atom additive protein force field:
1279 validation based on comparison to NMR data. *Journal of computational chemistry*
1280 **34**, 2135-2145, doi:10.1002/jcc.23354 (2013).

1281 51 Brooks, B. R. *et al.* CHARMM: the biomolecular simulation program. *Journal of*
1282 *computational chemistry* **30**, 1545-1614, doi:10.1002/jcc.21287 (2009).

1283 52 Wu, E. L. *et al.* CHARMM-GUI Membrane Builder toward realistic biological
1284 membrane simulations. *Journal of computational chemistry* **35**, 1997-2004,
1285 doi:10.1002/jcc.23702 (2014).

1286 53 Berendsen, H. J. C., Postma, J. P. M., Van Gunsteren, W. F., Di Nola, A. & Haak,
1287 J. R. Molecular Dynamics with Coupling to an External Bath. *J. Chem. Phys.* **81**,
1288 3684–3690 (1984).

1289 54 Darden, T., York, D. & Pedersen, L. Particle Mesh Ewald: An N·log(N) Method
1290 for Ewald Sums in Large Systems. *J. Chem. Phys.* **98**, 10089–10092 (1993).

1291 55 Hess, B., Bekker, H., Berendsen, H. J. C. & Fraaije, J. G. E. M. LINCS: A Linear
1292 Constraint Solver for Molecular Simulations. *J. Comput. Chem.* **18**, 1463–1472
1293 (1997).

1294 56 Grant, B. J., Rodrigues, A. P., ElSawy, K. M., McCammon, J. A. & Caves, L. S.
1295 Bio3d: an R package for the comparative analysis of protein structures.
1296 *Bioinformatics* **22**, 2695-2696, doi:10.1093/bioinformatics/btl461 (2006).

1297 57 Yu, H. & Dalby, P. A. A beginner's guide to molecular dynamics simulations and
1298 the identification of cross-correlation networks for enzyme engineering. *Methods*
1299 *in enzymology* **643**, 15-49, doi:10.1016/bs.mie.2020.04.020 (2020).

1300 58 Munteanu, C. R. *et al.* Solvent accessible surface area-based hot-spot detection
1301 methods for protein-protein and protein-nucleic acid interfaces. *Journal of*
1302 *chemical information and modeling* **55**, 1077-1086, doi:10.1021/ci500760m
1303 (2015).

1304 59 Kaech, S. & Banker, G. Culturing hippocampal neurons. *Nature protocols* **1**,
1305 2406-2415, doi:10.1038/nprot.2006.356 (2006).

1306 60 Jiang, M., Deng, L. & Chen, G. High Ca(2+)-phosphate transfection efficiency
1307 enables single neuron gene analysis. *Gene Ther* **11**, 1303-1311,
1308 doi:10.1038/sj.gt.3302305 (2004).

1309 61 Groc, L. *et al.* Differential activity-dependent regulation of the lateral mobilities of
1310 AMPA and NMDA receptors. *Nat Neurosci* **7**, 695-696, doi:10.1038/nn1270
1311 (2004).

1312 62 Heyer, M. P., Feliciano, C., Peca, J. & Feng, G. in *Genomics: Essential Methods*
1313 211–248 (John Wiley & Sons, Ltd, 2010).

1314 63 Edfawy, M. *et al.* Abnormal mGluR-mediated synaptic plasticity and autism-like
1315 behaviours in Gprasp2 mutant mice. *Nat Commun* **10**, 1431,
1316 doi:10.1038/s41467-019-09382-9 (2019).

1317 64 Matt, L. *et al.* SynDIG4/Prrt1 Is Required for Excitatory Synapse Development
1318 and Plasticity Underlying Cognitive Function. *Cell Rep* **22**, 2246-2253,
1319 doi:10.1016/j.celrep.2018.02.026 (2018).

1320 65 Fernandes, D. *et al.* Disrupted AMPA Receptor Function upon Genetic- or
1321 Antibody-Mediated Loss of Autism-Associated CASPR2. *Cereb Cortex* **29**, 4919-
1322 4931, doi:10.1093/cercor/bhz032 (2019).

1323 66 Zhang, H. *et al.* Modulation of AMPA receptor surface diffusion restores
 1324 hippocampal plasticity and memory in Huntington's disease models. *Nat*
 1325 *Commun* **9**, 4272, doi:10.1038/s41467-018-06675-3 (2018).
 1326